

A Near-Infrared Survey of the Inner Galactic Plane for Wolf-Rayet Stars III. New Methods: Faintest WR Stars

Graham C. Kanarek

Columbia University, New York, NY

Michael M. Shara

American Museum of Natural History

79th Street and Central Park West, New York, NY, 10024-5192

Jacqueline K. Faherty

Department of Terrestrial Magnetism, Carnegie Institution of Washington

5241 Broad Branch Road NW, Washington, DC 20015

David Zurek

American Museum of Natural History

79th Street and Central Park West, New York, NY, 10024-5192

Anthony F.J. Moffat

Département de Physique, Université de Montréal

CP 6128 Succ. C-V, Montréal, QC, H3C 3J7, Canada

ABSTRACT

A new method of image subtraction is applied to images from a J, K, and narrow-band imaging survey of 300 square degrees of the plane of the Galaxy, searching for new Wolf-Rayet stars. Our survey spans 150 degrees in Galactic longitude and reaches 1 degree above and below the Galactic plane. The survey has a useful limiting magnitude of $K = 15$ over most of the observed Galactic plane, and $K = 14$ (due to severe crowding) within a few degrees of the Galactic center. The new image subtraction method described here (better than aperture or even point-spread-function photometry in very crowded fields) detected several thousand emission-line candidates. In June and July 2011 and 2012, we spectroscopically followed up on 333 candidates with MDM-TIFKAM and IRTF-SPEX, discovering 89 emission-line sources. These include 51 Wolf-Rayet stars, 45 of them previously unidentified, including the most distant known Galactic WR stars, more than doubling the number on the far side of the Milky Way. We also demonstrate our survey's ability to detect very faint PNe and other NIR emission objects.

1. Introduction

In the more than 140 years since their first identification (Wolf & Rayet 1867), Wolf-Rayet (WR) stars have remained one of the most interesting (and, at times, baffling) classes of stars. Their huge masses ($\geq 25 M_{\odot}$ for initial stellar mass) and short lifetimes (typically $\sim 3 \times 10^5$ years in the WR phase) make them excellent tracers of recent star formation, and their position in the stellar evolutionary chain is important to both stellar astrophysics and supernova theory. The intense stellar winds of WR stars add a significant amount of C and O, and some N, to the interstellar medium (ISM), and contribute a significant fraction of the ISM’s energy and momentum budget; they also produce characteristic emission lines which give astronomers a probe into the atmospheres of these very hot, evolved stars.

The most reliable method to date of WR detection has been to look for narrowband excess due to emission lines in the optical, particularly the strong HeII 4686Å line. However, probing the Milky Way using this technique is difficult beyond ~ 3 kpc due to extreme dust extinction (~ 30 visual magnitudes across and through the center of the Galaxy); in the NIR only ~ 3 magnitudes of extinction occurs across the Galactic plane (see Shara et al. 1999, section 7). Clearly the NIR is the wavelength range of choice for searching out the vast majority of WR stars in the Milky Way. Two earlier papers in this series have focused on photometric techniques, and identified 112 new Galactic Plane WR star (Shara et al. 2009; Shara et al. 2012, hereafter Paper I and Paper II, respectively).

Simple models of the WR distribution in the Galaxy predict high concentrations near the Galactic center (Paper I), where extremely crowded images cause usual photometric techniques to fail. However, using a new method of image subtraction, along with NIR and MIR color-cuts we are able to significantly improve the selection criteria in the most crowded parts of the Galaxy; follow-up of candidates with this new technique produced 90 new emission-line sources in the Galactic Plane, including 55 new Wolf-Rayet stars. In section 2 we briefly describe the imaging survey and data reduction pipeline. Spectrographic follow-up data reductions are described in section 3, and the new candidates are presented in section 4. The resulting overall distribution of all known WR stars is presented and discussed in section 5. We briefly summarize our conclusions in section 6.

2. Survey & Data Reduction Pipeline

This survey was previously described in Paper I. More than 88,000 exposures were taken of the galactic plane on the CTIO 1.5-m telescope over approximately 200 nights during 2005-2006. The survey covers 1° above and below the Galactic plane, from longitudes -90° to 60° . The images are $35' \times 35'$, with $1''.03$ per pixel plate scale, in four narrowband filters as well as the *J* and *K* bands. The narrowband filter set is described in Paper I. The justification for the narrowband filters is: WCs can be discriminated using the ratio of the C IV 2.081 μ m filter to a 2.112 μ m He I line, and WNs with the ratio between the He II 2.192 μ m filter and each of the 2.112 μ m line and the 2.169 μ m

Br- γ filters.

The images from this survey were completely re-reduced for the new image-differencing pipeline described in this paper. Super dome flats for each month were created by combining all dome flats in that month. The images were then divided by the master dome flats. A skyflat was created by median-combining the first dither positions from all the separate pointings. The skyflat was then scaled to match each image in the dither sequence and subtracted. Next, DAOphot (Stetson 1987) was used to find sources in each of seven dither positions for every field. The sources were matched using DAOMatch and DAOMaster, and finally the 7 dither positions were combined using MONTAGE2 (Stetson 1994).

WCS astrometry for the images was computed by the astrometry.net package (Lang et al. 2010), using J and K index files with skymark diameter ranges from 8 to 11 arcmin. The program was called with xylists obtained by the NASA IDL Astronomy Library’s version of DAOphot’s FIND procedure (Landsman 1993), using the 500 brightest stars in each image. After including SIP distortion coefficients, mean residuals less than 0.5 arcsec were found when compared to 2MASS sources (Skrutskie et al. 2006). Then, working on a field-by-field basis, we computed photometry using the IDL-DAOphot procedures SKY, FIND, and APER, and the positions output by these routines were matched among the images. Sources were then matched to 2MASS source lists in J and K , and a mean magnitude offset calculated to calibrate the photometry library to 2MASS.

Once WCS solutions and photometry had been obtained, we performed image differencing in wavelength-space, which provided a method to find rare emission-line sources from very crowded images. We generated a continuum image for each emission-line-centered narrowband image (ENB) by linearly interpolating between the two continuum narrowband (CNB) images in wavelength space; this interpolated image (INB) was then subtracted from the emission line image to produce the residual. Images were subdivided to allow modeling of the spatially-varying sky background by an array of intersecting planes. After removal of the background, stellar positions in each subdivision were matched between images and a translation/rotation warp was applied to spatially align subdivisions as accurately as possible. Higher-order warp solutions were not found to improve alignment significantly.

After warping the subdivisions to match, we scaled the global brightness between the ENB and INB images. Through trial and error we concluded that no single method of determining a scaling factor worked for all images (or even all subdivisions); thus, to remove outliers, five different scaling factors were determined for each subdivision, using different methods. The final scaling factor was chosen as the median value of all methods on all subdivisions. No PSF matching was performed, as (a) each image had a PSF which displayed large spatial variations, and (b) the blurring due to convolution was generally catastrophic to the resolution of the images.

Once the ENB and INB images were matched as closely as possible, the difference image was obtained. Figure 1 shows the C IV ENB image (left) and difference image (i.e. on-line intensity including continuum, minus interpolated and scaled off-line continuum-only intensity, right) for field

1093, a typical field which lies 24° from the Galactic Center, and is relatively crowded, containing 6 previously known WR stars. The difference image in figure 1 demonstrates how both the spatially-varying sky and more than 99% of the stellar sources were removed by the subtraction process. Figure 2 shows a previously known WR star in that field. Despite the lack of PSF fitting, residual artifacts for the non-emission sources are quite minimal compared to the strong residual emission PSF of the WR star.

The final determination of candidates from the difference images involved a 3-step process. Each difference image contained many residuals that were the product of bad subtractions instead of true stellar-line emission; these must be removed. First, we determined the magnitude of every star which produced a significant positive residual in the difference image (m_{diff}), and normalized this magnitude by the original magnitude of the star in the CNB images ($m_c = (m_{C1} + m_{C2})/2$) to produce $\Delta m = m_{diff} - m_c$, a metric conceptually similar to equivalent width.

We then plotted m_c vs Δm for each filter, including a large number of fields on each plot, and determined isodensity contours. Then, m_c vs Δm was plotted for each filter in each individual field, and the 99% density contour was overlaid. Only those sources with significant bright deviations outside the 99% contour were considered as candidates, to eliminate field stars with no emission that survived the subtraction due to random fluctuations and poor PSF matches.

Figure 3 shows the Δm plot for the C IV filter in field 1093. Determining the optimal region of the Δm plot for strong WR characteristics was accomplished by plotting previously known Wolf-Rayet stars, and identifying areas where particular types seemed clustered, particularly with separation from the main density of residual field stars. By overplotting smoothed 99% density contours onto these diagnostic plots, we were able to isolate strong candidates for further refinement.

The second step of the selection process was to apply Mid-infrared (MIR) and Near-infrared (NIR) color cuts. We matched every source in each image to entries in the 2MASS and WISE (Wright et al. 2010) point source catalogs, and applied the following color cuts, as per Faherty et al. (2014):

$$\begin{aligned} J - K &< 3.23(H - K) - 0.296 \\ W1 - W2 &> 0.125(J - K) + 0.025 \end{aligned}$$

The left panel of figure 4 is a color-color diagram showing the NIR color cut, using 2MASS colors only. The great majority of WR stars lie below the cut line, while the great majority of field stars lie above it. In the right panel, a color-color plot including colors from the WISE photometry, the separation is even more pronounced. WR stars are intrinsically very hot, and therefore blue, and so it should come as no surprise that no WR stars lie below the cut line, with at least a 0.2 magnitude separation from the main bulk of field stars (chosen at random from the 2MASS and WISE catalogs). The physical reason for the positions of WR stars on the color-color diagrams in figure 4 is discussed in detail in Faherty et al. (2014).

Figure 4 also includes a selection of Galactic planetary nebulae (PNe), selected from the

Strasbourg-ESO catalog (Acker et al. 1992), which are one of the primary contaminants in the emission line candidate sample. The third and final step was to visually blink all candidates that both satisfied the color cuts and had significant deviations on the Δm plot; this method serves to remove PN contaminants which are resolved, and (along with other color cuts) removes the great majority of likely PNe from the candidate list.

3. Spectral Follow-up & Reduction

The first round of spectral follow-up for this candidate set was conducted over 7 nights at MDM and 12 half-nights at IRTF in June and July 2011.

3.1. IRTF

At the 3m NASA Infrared Telescope Facility (IRTF), we obtained NIR spectra of 150 candidate WR stars, selected using the criteria above, with the SpeX spectrograph. Two of the nights were cloudy enough to prevent observations. We operated in cross-dispersed mode with the 0.5" slit aligned and obtained an average resolving power of $\lambda/\Delta\lambda \sim 1200$, over a wavelength range of 0.8 – 2.4 μm .

We first acquired each target in the guider camera, then took a single AB dither pattern, with exposure times varying from 30s for our brightest targets to 200s for our faintest. Once we had confirmed the presence of emission lines we began a second set of AB images so each WR candidate had four images obtained with an ABBA dither pattern along the slit. To minimize the overhead (slew and calibration target time) between sources, we chose nearby subsequent targets.

After each several targets (typically 4-5), we observed an A0V star at a similar airmass for flux calibration and telluric correction. Internal flat-field and Ar arc lamp exposures were also acquired for pixel response and wavelength calibration, respectively. Additionally, we acquired spectra of almost all known spectral subtypes of Wolf-Rayet star. We reduced all data with SpeXtool version 3.3 (Vacca et al. 2004; Cushing et al. 2004) using standard settings.

3.2. MDM 2011

During a run of excellent weather over the 7 nights in June 2011, we obtained 113 NIR spectra of candidate stars using TIFKAM in spectroscopic mode on the 2.4m Hiltner telescope at MDM Observatory. The weather conditions were excellent, with average seeing $\sim 1.5''$. We operated with the 100 micron slit, the K blocking filter, and the J/K grism, providing wavelength coverage of 1.97 – 2.42 μm at a resolving power of $\lambda/\Delta\lambda \sim 660$. We performed a single AB dither pattern on each source once it had been placed on the slit in movie mode and a guide star acquired. If on-the-fly

extraction using IRAF showed emission, a second AB dither was taken, giving each WR candidate an ABBA dither pattern along the slit. Exposure times varied from 20s for the brightest targets to 240s for the faintest. We also observed A0V stars at a variety of airmasses for flux calibrations and telluric corrections, acquiring internal flat-field exposures as well for calibrating pixel response. Additionally, we obtained spectra of almost all known spectral subtypes of Wolf-Rayet star.

Spectra from this run were reduced with a combination of IRAF packages and IDL programs. Trimming and flat-fielding were performed with CCDPROC and FLATCOMBINE, and extraction was performed with APALL, all in IRAF. Image arithmetic, wavelength calibration, and combining extracted spectra were done in IDL; we used the XTELLCOR_GENERAL program included in the SpeXtool package, also written in IDL.

We discovered after the run that the NeAr arc lamp images we took at the telescope were faulty, and so wavelength calibration was performed using night sky lines taken from the unprocessed images. The resulting wavelength calibration is in some cases mediocre, but there was a good enough match to perform telluric corrections, as well as to assign WR star types and subtypes.

3.3. MDM 2012

During early 2012, the original survey data were reduced again, using different methods to produce better images. A new IDL pipeline was constructed, creating flat and sky images by median-combining the first and last dither of each pointing for the entire month, using high-quality data images instead of relatively poor dome flats. Then, during a 10-day observing run in the summer of 2012 (with 6 usable nights), we obtained 70 additional NIR spectra of candidate stars with TIFKAM at MDM, with the same instrument setup as in 2011.

Reductions were performed entirely in IRAF, primarily using the KPNOSLIT and ONEDSPEC packages. We used a selection of long and short exposure flats to create a bad pixel mask with CCDMASK, and then performed trimming, bias-subtraction, and flat-fielding with FLATCOMBINE and CCDPROC. Once the initial preparation was complete, the spectra were extracted from the A-B images with APALL. Then we used IDENTIFY to determine a wavelength solution for each spectrum from the 4 or 5 strong Ar lines, and DISPCOR to apply the solutions to the spectra. All spectra for each individual object were combined using SCOMBINE, and then telluric correction was performed with TELLURIC.

4. Results

During 29 nights of observing we observed 333 candidates, finding 89 NIR emission sources (for a success rate of 27%) in some of our survey’s most crowded fields. Of the emission-line sources, 51 were WR stars, 45 of which had never been previously identified, with 24 WC and 27 WN;

finder charts for these new WR stars are included in appendix A. WR types and subtypes were assigned by eye, comparing the relative strengths of nearby line pairs as in Crowther et al. (2006a); classification would ideally be performed using EWs of the spectral lines, but in many cases they are difficult to obtain due to heavy blending which is easily compensated for by eye. Figures 5 and 6 show the positions of the new emission sources on the color cut plots, and figures 7 thru 15 show the spectra of the new WR stars, sorted by subtype. Tables 2 through 6 give the location, magnitude, subtype, and (in some cases) extinction and distance of each NIR emission object classified in this paper.

One of the confirmed WR stars is particularly notable: WR1627-A6D, a WC7:: which is associated with a Chandra x-ray source (CXO J191011.5+085839); no other WRs described here were successfully matched to Chandra sources. WR1627-A6D was originally identified in Smith et al. (2012), also as a WC7. Using the relation $A_K/A_V = 0.112$ from Rieke & Lebofsky (1985) with the calculated A_K of 3.00, we derive a V -band extinction of 26.8 for $R = 3.11$ extinction. Then, we derive the hydrogen column density as in Predehl & Schmitt (1995), arriving at $N_h = 4.82 \times 10^{22} \text{ cm}^{-2}$. This source has an ACIS-broad x-ray flux of $3.1 \times 10^{-14} \text{ erg s}^{-1} \text{ cm}^{-2}$, and assuming a characteristic temperature of 1 keV, an unabsorbed flux of $4.1 \times 10^{-13} \text{ erg s}^{-1} \text{ cm}^{-2}$ (calculated via WebPIMMS¹). Using the calculated distance shown in table 6, we find an x-ray luminosity of $1.7 \times 10^{33} \text{ erg s}^{-1}$, which is consistent with other WN x-ray luminosities, but two orders of magnitude higher than the WCs in Skinner et al. (2006). For a characteristic temperature of 3 keV, this becomes an unabsorbed flux of $1.0 \times 10^{-13} \text{ erg s}^{-1} \text{ cm}^{-2}$ and an x-ray luminosity of $3.4 \times 10^{32} \text{ erg s}^{-1}$; if the characteristic temperature is 10 keV, the unabsorbed flux would be $7.6 \times 10^{-14} \text{ erg s}^{-1} \text{ cm}^{-2}$, for an x-ray luminosity of $2.5 \times 10^{32} \text{ erg s}^{-1}$. There are no known single WC stars which show x-ray emission; this fact coupled with the relatively high x-ray luminosity for a WC star raises, but does not prove, the possibility of a compact companion.

In addition to new WR stars, we classified a number of other emission-line objects which were selected using our tools. The 17 planetary nebulae (spectra shown in figure 16) display strong emission in the He I 2.06 μm and Br- γ /He I 2.17 μm filters, with little to no continuum. PNe are quite easy to identify, particularly using 2MASS and WISE color criteria, as described in Faherty et al. (2014) and a paper in preparation. We also observed nine emission-line sources which are likely to be emitting YSOs (cf. Greene & Lada 1996) due to the lack of CO bands redwards of 2.3 μm ; these spectra are shown in figure 17.

Another source of interlopers in the WR candidate set is Be stars (see also Faherty et al. 2014; Mauerhan et al. 2010); the 5 Be spectra are shown in figure 18. These spectra show relatively weak emission in the 2.17 μm filter, with strong continuum emission and a large number of hydrogen lines, especially in the H-band. Finally, the largest category of contaminants among our candidates are M giants and supergiants, often with Br- γ emission, as shown in figures 19 and 20 (cf. Rayner et al. 2009). Contaminants with no emission were generally chosen using criteria from the He II and

¹<https://heasarc.gsfc.nasa.gov/cgi-bin/Tools/w3pimms/w3pimms.pl>

Br- γ filters early on in the selection process; due to the shape of the spectra, these stars appeared brighter in those filters than in at least one of the continuum filters. Once we discovered this trend, that criterion was no longer used.

5. Galactic WR Distribution

We expect to find WR stars in areas with recent star formation, which in spiral galaxies like the Milky Way will be in the plane of the Galaxy, concentrated most closely along the spiral arms. Figure 21 shows a plot of the distribution of confirmed WR stars as projected onto the sky, using coordinates from the Wolf-Rayet Catalogue VIII, maintained by Paul Crowther, and absolute magnitude calibrations for the various WR types as in Rosslowe & Crowther (2013). As expected, the WR stars cluster strongly within 1° of $b = 0$; 80% of all confirmed WR stars lie within the bounds of the survey described in section 2, despite being limited to $\pm 1^\circ$ in Galactic latitude. Also included in figure 21 is a histogram showing the distribution of WR stars in Galactic longitude. The plot shows heavy clustering at $l = \pm 30^\circ$, where the telescope is pointed along the Carina or Norma arms, as predicted in simulations of WR distribution based on local surface densities, described in the appendix to Paper I.

Figure 22 shows the distribution of WR stars on the Galactic plane, overlaid on an artist’s representation of the Milky Way so as to highlight the spiral arms. This work (in combination with Papers I and II) more than doubles the number of confirmed WR stars on the far side of the Galaxy, including the most distant WR stars yet identified. The majority of new WR stars classified here roughly trace the northern curve of the Carina arm, where one would expect the most massive star formation.

5.1. Completeness and the Survey in Context

The image subtraction methods detailed in section 2, in addition to the candidate selection methods described in Papers I and II, have allowed us to identify the faintest, furthest WR stars in the Galaxy. Figures 23 and 24 show histograms and cumulative fractions of the J- and K-magnitudes, respectively, for WR stars identified by the Shara et al. survey and in the literature. There is a clear divergence in the range of typical magnitudes between the two populations; the WR stars identified by this survey are significantly fainter than those in the literature, particularly for WC stars, which can be far more difficult to identify if the emission lines are diluted by continuous NIR emission by the star’s shroud of dust (a characteristic of WC9ds, particularly near the Galactic center). In addition, figure 25 shows that these faint WR stars lie at greater distances from the Solar System than any WR stars previously identified. The Shara et al. survey has more than doubled the number of confirmed WR stars on the far side of the Milky Way.

As a check on the reasonability of our distance calculations, we plotted K-band absorption

vs 2MASS K magnitude in figure 26. Included is a least-absolute-deviation linear fit, which, as expected, shows the increase of absorption with K magnitude (as a directly-observable analogue for distance) for both WN and WC stars, as well as a combined plot for all WR stars.

This imaging survey [Paper I, Paper II, and the present paper] has contributed 27% of the currently identified population of Galactic WR stars. The majority of this contribution lies in regions that have not been explored previously in the literature, particularly in magnitude/color space. Figure 27 shows all currently-known WRs on an NIR color-magnitude diagram. Before this survey, it might have been believed that such a diagnostic would be effective at isolating candidate WR stars, as the great majority of WRs from the literature are separated from the main field star region. However, when the results from this survey are included, it's clear that Wolf-Rayet stars are found among the crowded field regions in this diagram, and that this survey is effectively identifying faint, reddened, distant WR stars.

The set of new WR stars and other emission objects presented in this paper is not complete, nor was there any attempt at completeness; the criteria by which we selected WR candidates evolved continuously throughout the follow-up observations. Instead these new WR stars serve as a test for the image subtraction method as a means of identifying new WR stars in the survey images which had already been probed by Papers I and II. These new WR stars are a valuable addition to the catalogue of Galactic WR stars, and measures of completeness will be discussed in the next paper in this series, in preparation.

6. Conclusions & Looking Forward

The imaging survey first introduced in Paper I has already produced 27% of the known Galactic WR stars using photometric selection techniques (Shara et al. 2009; Shara et al. 2012). Using new reductions and image-subtraction methods, we have shown in this paper that there are still many more Galactic WR star candidates to be discovered and confirmed, particularly in the Southern hemisphere. The Galactic Center region in particular has not been tapped, as the survey images are so crowded that special care must be taken with them. The pipeline described in this paper is capable of analyzing all but the densest regions in our survey.

The WR population simulations presented in Paper I predicted several thousand WR stars in the Milky Way, which have not yet been identified. However, the results presented here are not inconsistent with those predictions, for a few reasons. First, due to the necessity of spectroscopic follow-up to confirm each WR star, even with a high success rate the number of observations necessary is very large. Second, the majority of WR stars still unidentified lie either on the far side of the Galaxy, and are thus very faint, or near the Galactic Center in prohibitively crowded fields.

This publication makes use of data products from the Two Micron All Sky Survey, which is a joint project of the University of Massachusetts and the Infrared Processing and Analysis Center/California Institute of Technology, funded by the National Aeronautics and Space Admin-

istration and the National Science Foundation. This publication also makes use of data products from the Wide-field Infrared Survey Explorer, which is a joint project of the University of California, Los Angeles, and the Jet Propulsion Laboratory/California Institute of Technology, funded by the National Aeronautics and Space Administration. AFJM is grateful for financial assistance from NSERC (Canada) and FRQNT (Quebec).

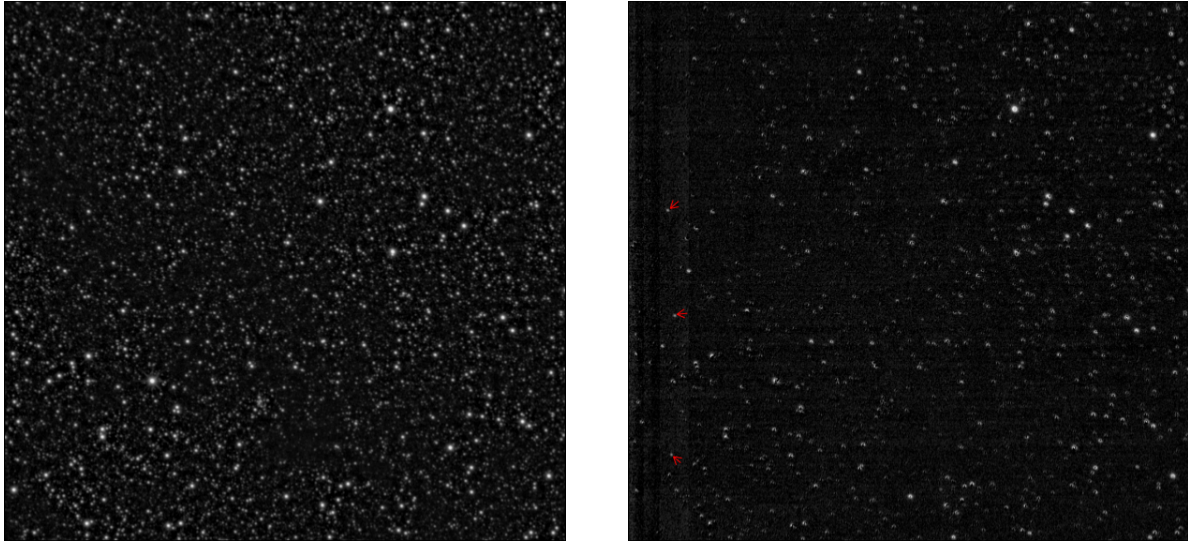


Fig. 1.— A quadrant of the C IV image from field 1093 (a representative survey field), before (left) and after (right) image differencing, subtracting a narrow-band continuum image scaled to the same wavelength and intensity, so that most stars should subtract to zero. This image demonstrates the high degree of crowding present in the survey images (the displayed field is ~ 24 deg from the Galactic center). Residuals ideally are candidate emission objects. The great majority of point sources have been completely removed; residual flux from most of the remaining non-emission stars is due to incomplete subtractions of saturated stars ($K \leq 9$), or from inadequate PSF matching due to high spatial variability in the PSF between and within the images. Three previously-known WR stars from the literature are identified with red arrows in the difference image.

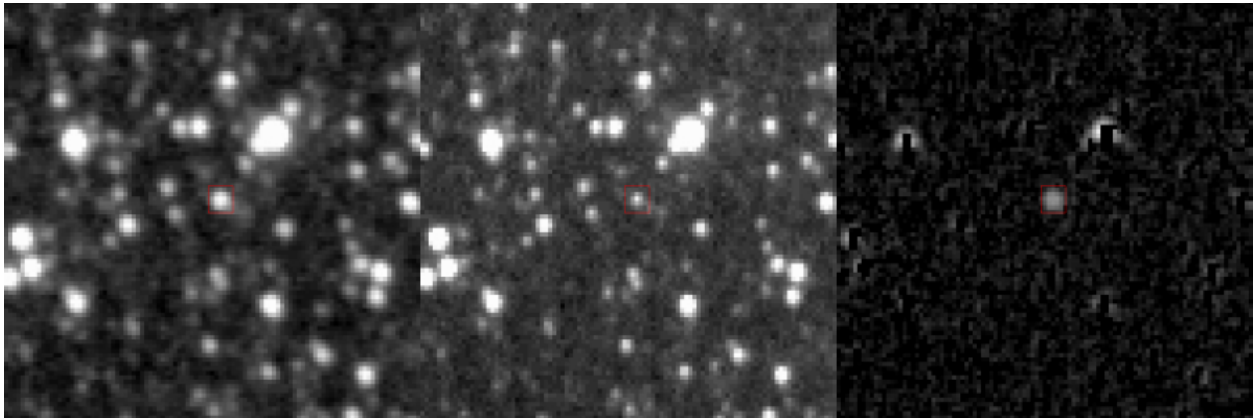


Fig. 2.— A zoomed portion of the image in figure 1, highlighting a known WR star in the C IV narrow band image (left), C IV interpolated continuum image (center), and difference image (right). The WR star remains as a perfect residual PSF in the difference image, while the great majority of source pixels elsewhere are removed by the subtraction process, leaving only the brightest sources in the original C IV image as incomplete subtractions.

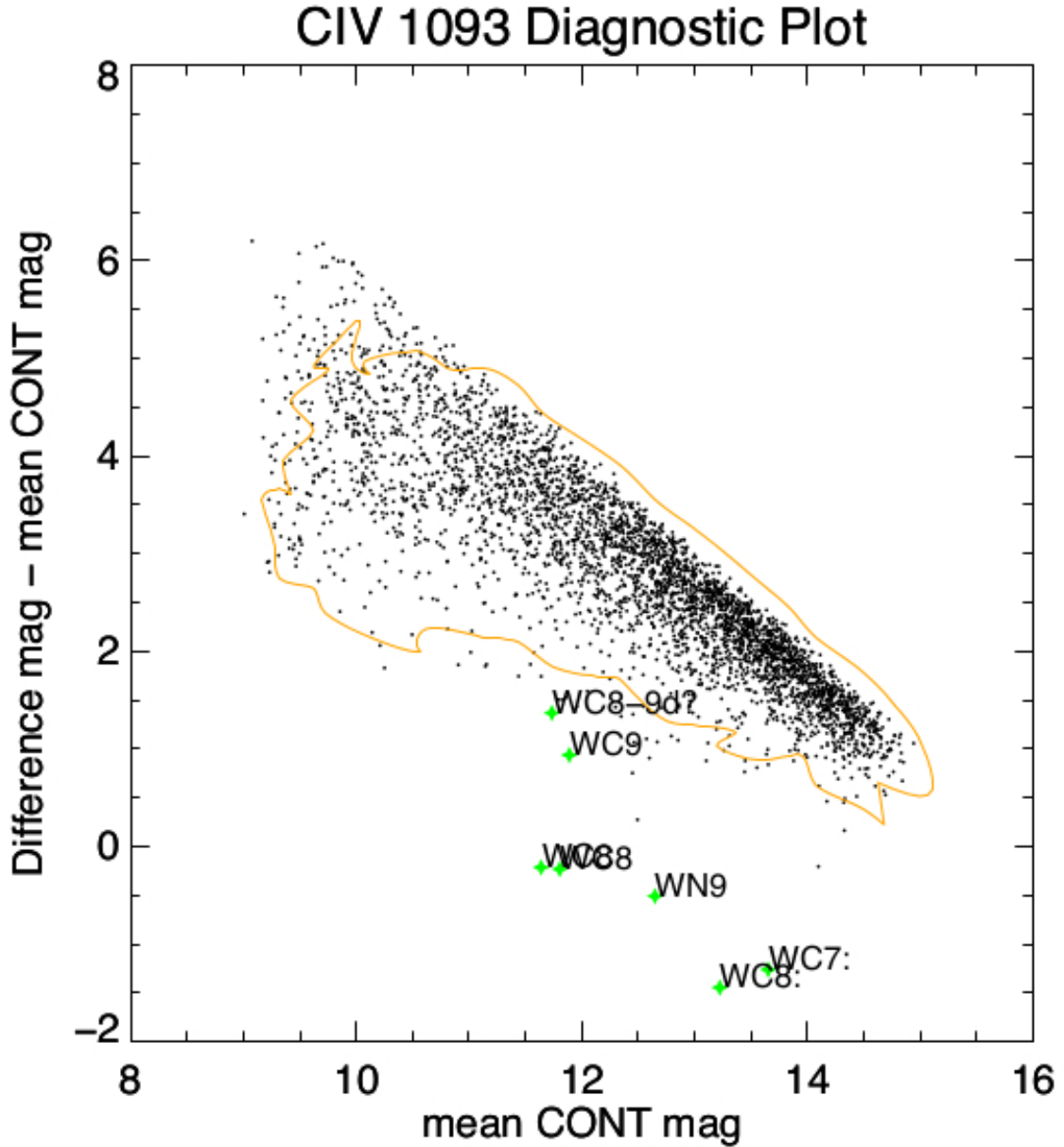


Fig. 3.— The diagnostic (“ Δm ”) plot for field 1093, in the CIV filter (the the image shown in figures 1 and 2). The difference image magnitude (m_{diff}) on the y -axis has been normalized for the original source brightness by subtracting continuum magnitude (m_c), leaving Δm the normalized emission-line excess. By enclosing 99% of the points in the orange isodensity contour, we isolate those sources with excess that are least likely to be incomplete subtractions; known WR stars in this field, the green labeled points, lie well outside the contour. To survive the culling process, prospective candidates must lie below the contour, in a similar region to the WRs from the literature.

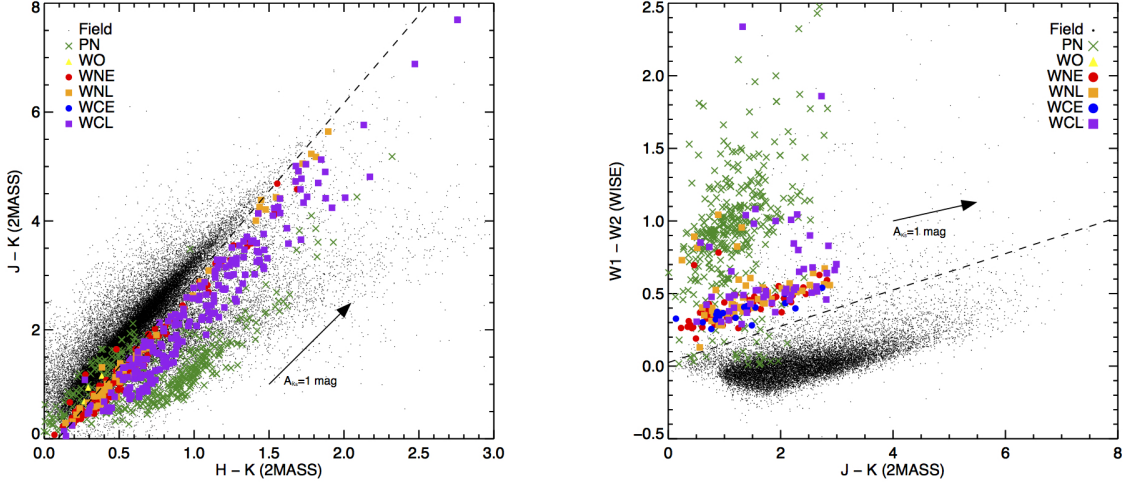


Fig. 4.— The second diagnostic tool for candidate selection: color cuts from NIR (2MASS) and MIR (WISE) magnitudes. These are analogous to the figures in Mauerhan et al. (2011), described in more detail in Faherty et al. (2014). These plots provide another layer of differentiation during the selection process. The right plot in particular shows the wide separation between emission objects (WR stars and PNe) and field stars in NIR/MIR color space. PNe are included as common emission objects other than WR stars which can be found using these tools; 18 newly-identified PNe are presented in this paper. $A_{K_s} = 1$ reddening vectors have been added, using the values for $A_{[\lambda]}/A_K$ from Indebetouw et al. (2005); the values for [3.6] and [4.5] were used for WISE filters W1 and W2, as the central wavelengths are sufficiently similar.

Table 1. Predicted candidate strength in survey filters

Filter Name	He I	C IV	Br- γ /He I	He II
Early WN	none - very weak	none ^a	weak	strong - very strong
Late WN	very strong	none ^a	very strong	weak - strong
Early WC	weak - strong	very strong	none	none - very weak
Late WC	weak - strong	very weak - weak	very weak	none - weak
WO	none	weak	strong	weak

^aWNs may be detected in the C IV filter due to the wings of a strong He I line. This is a much more likely occurrence in WNLs than WNEs because of the relative strength of the He I line.

Table 2. Spectroscopically-Confirmed Wolf-Rayet Stars

Name	α (J2000)	δ (J2000)	l	b	Type ^a	Observed
1040-B6C	16 04 03.76	-53 10 44.2	-30.54	-0.527	WN9	IRTF
1089-1117	16 31 37.79	-48 14 55.3	-23.98	-0.038	cLBV/WNL ^b	IRTF
1093-1765	16 32 25.70	-47 50 46.1	-23.60	0.139	WN6	IRTF
1139-49EA	16 54 08.46	-43 49 25.3	-18.09	-0.073	WC6::	IRTF
1178-66B	17 07 23.95	-39 19 54.4	-13.02	0.738	WC9	IRTF
1176-B49	17 12 34.87	-40 37 13.8	-13.47	-0.827	WN9h	IRTF
1198-6EC8	17 15 55.90	-37 19 12.0	-10.41	0.575	WC6::	IRTF
1256-1483A	17 40 59.36	-32 11 22.1	-3.292	-0.860	WN9	IRTF
1319-3BC0	17 57 16.87	-25 23 13.8	4.376	-0.416	WC7:	IRTF
1338-2B3	17 59 07.99	-22 36 43.0	6.991	0.605	WN9	MDM12
1343-284	18 03 28.37	-22 22 58.9	7.686	-0.152	WN8-9	MDM12
1353-160A	18 05 35.60	-21 04 23.3	9.069	0.061	WC8-9	MDM12
1366-438	18 05 55.27	-19 29 44.1	10.483	0.765	WN7-8	MDM12
1367-638	18 09 06.22	-19 54 27.2	10.487	-0.090	WN9	IRTF
1381-19L	18 12 02.41	-18 06 55.4	12.392	0.167	WC9	MDM11
1389-4AB6	18 14 14.09	-17 21 02.6	13.313	0.075	WC7	IRTF
1389-1F5D	18 14 17.37	-17 21 54.4	13.307	0.057	WN8	IRTF
1446-B1D	18 25 00.25	-10 33 23.5	20.536	0.983	WN6 ¹	IRTF
1457-673	18 31 06.65	-09 48 01.4	21.904	0.004	WC9	MDM12
1485-6C4	18 36 55.53	-06 31 02.1	25.480	0.241	WN6	MDM12
1485-844	18 37 51.82	-06 31 19.1	25.583	0.032	WN8	MDM12
1495-1D8A	18 39 40.60	-05 35 17.6	26.620	0.059	WC8-9	MDM12
1495-705	18 39 41.19	-05 57 36.3	26.290	-0.113	WN8	MDM12
1514-AA0	18 41 06.79	-02 56 01.0	29.144	0.957	WC8	IRTF
1509-2E64	18 42 26.61	-03 56 36.0	28.398	0.199	WC9	IRTF
1525-2352	18 45 14.63	-02 05 05.7	30.370	0.427	WC8:	IRTF
1519-E43	18 45 49.88	-02 59 56.0	29.624	-0.121	WC7 ²	MDM12
1530-8FA	18 46 00.97	-01 14 35.0	31.207	0.639	WN5	IRTF
1541-3C8	18 50 02.75	-00 32 07.9	32.297	0.066	WC8 ²	MDM11
1541-197C	18 50 37.54	-00 01 21.1	32.819	0.171	WC8	MDM11
1544-FA4	18 51 33.09	-00 13 40.8	32.742	-0.129	WN5	IRTF
1547-1DF2	18 51 38.98	-00 10 08.1	32.806	-0.124	WN8:	MDM11
1553-9E8	18 52 33.12	+00 47 41.8	33.766	0.115	WN9h	MDM11
1547-1488	18 52 57.20	+00 02 54.1	33.148	-0.315	WN5	IRTF
1553-15DF	18 53 02.56	+01 10 22.7	34.159	0.178	WC8	IRTF
1602-9AF	19 02 42.32	+06 54 44.4	40.365	0.657	WN6	MDM11

Table 2—Continued

Name	α (J2000)	δ (J2000)	l	b	Type ^a	Observed
1603-11AD	19 04 20.14	+06 07 52.2	39.856	-0.061	WN5	IRTF
1609-1C95	19 06 10.68	+07 19 13.3	41.123	0.078	WC9	IRTF
1626-4FC8	19 06 33.66	+09 07 20.8	42.767	0.822	[WC6:] ^c	IRTF
1629-14D6	19 10 06.40	+09 45 25.7	43.733	0.339	WN9h	IRTF
1627-A6D	19 10 11.53	+08 58 39.6	43.051	-0.040	WC7:: ²	IRTF
1635-AD8	19 13 19.19	+09 55 29.0	44.248	-0.285	WN6	IRTF
1653-FFE	19 14 40.73	+11 54 15.4	46.156	0.338	WN5-6	IRTF
1651-BB4	19 15 37.26	+11 25 26.3	45.838	-0.089	WN5	IRTF
1647-1E70	19 15 52.52	+11 12 59.7	45.683	-0.241	WC8:	IRTF
1659-212	19 17 22.20	+12 13 09.2	46.741	-0.097	WN9	MDM12
1669-3DF	19 18 31.35	+13 43 39.4	48.206	0.360	WN9h	IRTF
1660-1169	19 20 02.46	+12 08 20.3	46.975	-0.712	WC6:	IRTF
1697-38F	19 25 18.12	+17 02 15.9	51.895	0.477	WC9	IRTF
1702-23L	19 26 08.35	+17 46 23.1	52.637	0.651	WC8	MDM11
1695-2B7	19 27 17.98	+16 05 24.6	51.289	-0.394	WC9	IRTF

^aIt is difficult to differentiate between features of WC4 – 8. A colon (:) indicates an uncertainty of up to ± 2 subtypes.

^bOriginally identified as a B[e]/LBV in Wachter et al. (2011), and then re-classified as a cLBV transitioning to late WN in Stringfellow et al. (2012).

^cOriginally classified as a [WC] in Gvaramadze et al. (2010).

¹Originally identified in Hadfield et al. (2007).

²Originally identified in Smith et al. (2012).

Table 3. Other NIR Emission Sources

Name	α (J2000)	δ (J2000)	l	b	Type ^a	Observed
1127-75C4	+17 29 37.54	-35 13 43.8	-7.126	-0.515	True PN ¹	IRTF
1235-8F56	+17 31 50.69	-34 10 44.3	-5.999	-0.319	PN	IRTF
1294-79B5	+17 46 01.68	-27 26 01.3	1.33	0.706	Possible PN ²	IRTF
1287-9C01	+17 47 14.65	-28 26 48.8	0.603	-0.05	PN	IRTF
1313-4913	+17 52 59.34	-25 27 28.1	3.825	0.385	Likely PN ²	MDM12
1326-4DC7	+17 56 28.55	-24 00 27.1	5.477	0.435	Be	IRTF
1312-111ED	+17 56 41.57	-26 31 09.5	3.33	-0.869	PN	IRTF
1338-18F	+17 58 57.24	-22 20 24.6	7.206	0.776	^a	MDM12
1331-65D3	+17 59 42.43	-23 51 43.7	5.972	-0.132	PN	IRTF
1343-69E	18 02 22.35	-22 38 00.3	7.343	-0.055	B[e]/LBV ^b	MDM12
1343-7F1	+18 02 44.42	-22 19 36.7	7.651	0.023	^c	MDM12
1353-3108	+18 04 08.45	-20 57 05.8	9.009	0.416	Likely PN ³	MDM12
1352-1192	+18 06 40.77	-21 40 17.4	8.67	-0.452	Be	IRTF
1407-E01	+18 18 58.19	-15 49 37.9	15.193	-0.198	^a	MDM12
1430-AB0	18 21 02.92	-12 27 45.8	18.397	0.945	PN ^d	IRTF
1442-59DB	+18 24 07.91	-11 06 42.6	19.945	0.913	True PN ²	IRTF
1443-760	18 28 33.39	-11 46 44.2	19.860	-0.358	B[e]/LBV ^b	IRTF
1457-472	+18 29 40.38	-09 31 21.5	21.986	0.447	^c	MDM12
1485-5BE	+18 36 16.87	-06 43 17.6	25.225	0.289	^c	MDM12
1485-95A	+18 37 14.85	-06 44 44.4	25.314	0.065	^c	MDM12
1489-1D47	+18 37 30.41	-06 14 15.0	25.795	0.241	PN	IRTF
1510-224	+18 39 43.87	-03 34 43.5	28.412	0.968	^c	MDM12
1499-691	+18 40 36.84	-05 27 24.5	26.843	-0.088	^c	MDM12
1510-2A8	+18 41 33.60	-03 39 05.9	28.556	0.529	^a	MDM12
1511-30E	+18 44 05.00	-03 57 02.4	28.578	-0.168	^c	MDM12
1511-98F	+18 44 18.19	-04 05 07.1	28.483	-0.278	^c	MDM12
1523-620A	+18 47 00.40	-02 27 51.6	30.234	-0.138	Possible PN ⁴	IRTF
1527-318B	+18 48 29.26	-02 10 01.4	30.667	-0.332	Possible PN ⁴	IRTF
1541-4EAC	+18 49 45.18	-00 29 08.0	32.308	0.154	PN	MDM11
1633-32F	+19 10 37.97	+09 47 34.5	43.824	0.240	^a	MDM12
1631-598D	+19 10 56.59	+09 28 36.6	43.579	0.026	PN	IRTF
1648-2717	+19 16 30.50	+10 40 56.3	45.283	-0.628	PN	IRTF
1702-13C	+19 25 15.87	+17 31 40.7	52.323	0.718	^c	IRTF
1697-173E	+19 25 53.53	+16 53 31.5	51.834	0.284	Likely PN ⁴	IRTF
1717-203	+19 30 57.41	+19 29 51.8	54.698	0.473	^a	IRTF
1704-2C5	+19 32 03.38	+16 44 42.4	52.411	-1.082	^a	MDM12
1734-1187	+19 32 28.69	+21 11 30.4	56.354	0.976	Be	IRTF
1764-165F	+19 45 32.87	+23 28 10.4	59.823	-0.536	Likely PN ⁴	MDM12

^aThese stars are emitting cool stars, M giants or supergiants (Rayner et al. 2009).

^bOriginally identified in Wachter et al. (2011).

^cA number of emission sources seem likely to be YSOs (Greene & Lada 1996).

^dThis object is missing the P Cygni absorption lines normally seen in a WN7h, and so is likely a high-ionization nebula.

¹Originally identified in Miszalski et al. (2008).

²Originally identified in Acker et al. (1992).

³Originally identified in Kerber et al. (2003).

⁴Originally identified in Urquhart et al. (2009).

Table 4. Photometry for Confirmed WR Stars

Name	B^a	V^a	R^a	J^a	H^a	K^a	$W1^a$	$W2^a$	$W3^a$	$W4^a$
1040-B6C	–	–	–	13.13	11.90	11.17	10.41	10.15	10.74*	8.35*
1089-1117	–	–	–	16.57*	12.60	10.28	8.53	7.53	6.58	1.62
1093-1765	–	–	–	15.15	12.93	11.57	10.46	9.98	8.71	8.55*
1139-49EA	–	–	–	16.29*	14.53*	13.09	–	–	–	–
1178-66B	–	–	–	12.49	11.12	10.26	9.51	9.03	8.40	6.99
1176-B49	–	–	–	12.66	11.22	10.41	9.69	9.24	8.81	7.86*
1198-6EC8	–	–	–	16.15*	14.68*	13.47	–	–	–	–
1256-1483A	–	–	–	13.98	12.46	11.86	11.07	10.81	4.89	0.84
1319-3BC0	–	–	–	14.89*	12.72*	11.46*	10.89	10.39	8.97*	7.58*
1338-2B3	–	–	–	12.61	10.48*	9.21*	–	–	–	–
1343-284	17.39	15.60	14.72	10.47	9.600	9.02	8.40	8.08	7.68	5.82*
1353-160A	–	–	–	14.11	12.20	11.14	10.09	9.85	9.80*	8.08*
1366-438	–	–	–	12.91	10.58*	9.20*	7.78	7.26	5.98	4.65
1367-638	–	–	–	15.96*	12.43	10.40	–	–	–	–
1381-19L	15.48	13.86	13.78	9.66	8.26	7.80*	7.34*	6.62	5.90	4.89
1389-4AB6	–	–	20.74	16.13	14.26	12.24	10.22	9.36	8.37	6.88
1389-1F5D	–	–	–	17.57*	13.28	11.05	9.67	8.79	8.91	5.78*
1446-B1D	–	–	17.24	12.21	11.24	10.61	9.68	9.31	8.30	6.95
1457-673	–	–	–	14.85*	11.44	9.35	7.55	6.66	5.28	3.62
1485-6C4	–	–	16.66	12.04	10.81	10.02	9.23	8.90	8.06	5.30*
1485-844	–	–	–	14.72	11.30	9.49	8.07	7.40	6.84	5.30
1495-1D8A	–	–	–	14.64*	12.36*	11.72	9.72	9.22	9.87	6.75
1495-705	–	–	–	14.97	11.38	9.16	7.31	5.92	4.75	3.77
1514-AA0	–	–	–	12.92	11.24	10.54	10.06	10.13	10.15	7.27*
1509-2E64	–	–	–	15.78*	14.87*	12.45	9.83	9.01	8.33	6.36*
1525-2352	–	–	–	17.93*	14.75	12.44	10.34	9.53	9.01*	6.23*
1519-E43	–	–	–	13.65*	13.04	11.26	9.59	9.01	9.66*	7.09*
1530-8FA	–	–	–	12.76	11.43	10.64	9.03	8.72	9.90	7.82*
1541-3C8	–	–	–	16.98*	13.86	12.15	10.73	10.06	8.54*	6.28*
1541-197C	–	–	–	14.74*	13.33	11.64*	10.05	9.30	8.73	4.45
1544-FA4	–	–	–	13.50*	12.24	10.83	9.61	9.02	8.37	7.17*
1547-1DF2	–	–	–	14.20	12.50	11.76	10.66	9.97	4.01	1.27
1553-9E8	–	–	–	15.76	12.86	10.98	9.54	8.54	8.47	6.35*
1547-1488	–	–	–	13.96	12.25	11.16	9.99	9.51	8.62	7.39*
1553-15DF	–	–	–	17.78*	14.80	12.07	9.70	8.62	8.28*	4.03
1602-9AF	–	–	–	13.11	11.62	11.05	10.59	10.67	9.60	7.27

Table 4—Continued

Name	B^a	V^a	R^a	J^a	H^a	K^a	$W1^a$	$W2^a$	$W3^a$	$W4^a$
1603-11AD	–	–	–	16.13	13.64	12.16	10.43	9.80	8.76	6.93
1609-1C95	–	–	–	18.41*	15.0*	11.93	9.91	8.35	8.58	8.19*
1626-4FC8	–	–	17.40	15.59	14.86	13.89	12.77	11.79	5.71	2.09
1629-14D6	–	–	–	14.73	13.44	12.63	11.75	11.40	10.42*	7.93*
1627-A6D	–	–	–	15.78*	13.54*	11.75	10.51	9.80	10.92*	6.77*
1635-AD8	–	–	–	15.20	12.87	11.48	10.27	9.63	9.26	8.52
1653-FFE	–	–	–	15.22*	13.00*	11.66*	10.37	9.78	9.17	8.61*
1651-BB4	–	–	–	15.83	13.21*	11.78*	10.30	9.53	8.60	5.18
1647-1E70	–	–	–	17.53*	15.10	12.57	10.74	9.66	8.65	4.93
1659-212	–	–	–	13.44	10.89	9.53	8.56	8.00	7.06	6.00
1669-3DF	–	–	–	12.79	11.03	9.97	8.81	8.22	7.61	6.57
1660-1169	–	–	–	14.65	13.29	12.08	11.65	11.22	11.15*	8.72
1697-38F	–	–	–	12.97	11.18	9.92	8.54	7.87	7.58	6.57
1702-23L	20.44	17.29	16.15	11.86	10.97	10.21	9.66	9.26	8.60	7.62
1695-2B7	–	–	–	13.01	11.09	9.64	8.40	7.70	7.27	7.02

^a B , V , and R photometry is from the NOMAD catalog; J , H , and K photometry is from 2MASS; and $W1 - 4$ are from the WISE preliminary source catalog. Questionable magnitudes (due to poor photometry, blending, contaminants, etc) and lower limits are marked with an asterisk*.

Table 5. Photometry for Other NIR Emission Sources

Name	B^a	V^a	R^a	J^a	H^a	K^a	$W1^a$	$W2^a$	$W3^a$	$W4^a$
1127-75C4	–		16.08	14.99	13.92	12.24	–		–	–
1235-8F56	–		–	16.48*	13.85*	12.7	–		–	–
1294-79B5	–		–	13.44*	12.44	11.57	10.18	9.63	4.33	0.54
1287-9C01	18.42	17.24	16.97	14.76	14.19*	12.02*	8.36	5.02	0.81*	1.68*
1313-49I3	–		16.01	13.45	12.79	11.8	9.9	9.33	4.08	-0.36
1326-4DC7	–		–	13.91	12.68	11.4	9.12	8.01	5.46	4.11
1312-111ED	–		–		–		–		–	–
1338-18F	–		–	14.32	11.48	9.88	8.37	7.69	7.19	6.55
1331-65D3	–		–	15.69	13.43*	12.51*	11.82	12.06	6.06	1.89
1343-69E	–		–	13.60	11.07	9.59	8.46	7.72	6.67	3.64
1343-7F1	–		–	13.99*	11.57	9.47	8.21	7.38	6.5	4.72
1353-3108	–		–	13.82	12.8	11.40	–		–	–
1352-1192	–		18.13	12.99	12.05	11.41	10.56	10.30	10.29*	7.40*
1407-E01	19.16	–	16.19	13.72*	11.61	9.98	8.7	8.18	7.55	7.47*
1430-AB0	17.07	15.21	16.90	11.70	11.11	10.64	9.92	9.63	9.12	8.19*
1442-59DB	–		–	14.35	13.85	12.63	10.17	9.62	4.79	1.69
1443-760	18.40	–	14.38	14.35	11.41	9.7	8.33	7.42	6.72	2.93
1457-472	–		–	10.59	10.19	9.84	9.14	8.82	7.7	5.85
1485-5BE	13.47	13.10	12.75	11.01	10.26	9.92	9.39	8.36	6.5	2.97
1485-95A	14.98	13.88	12.70	11.76*	10.80*	10.34	9.77	9.59	9.42*	6.31*
1489-1D47	17.34	16.14	14.80	14.08	12.12	10.62	7.55	6.52	1.21	-2.04
1510-224	–		–	10.1	8.43	7.56	6.95	6.53	4.93	3.72
1499-691	–		–	10.86	9.94	9.29	8.67	8.41	8.57	6.96*
1510-2A8	18.79	17.69	15.52	11.1	9.29	8.25	7.32	6.85	6.59	6.37
1511-30E	–		18.08	9.98	9.63	9.55	9.33	9.31	8.84*	5.54*
1511-98F	12.16	11.73	11.44	11.13	10.84	10.66	10.38	10.38	9.05*	6.70*
1523-620A	13.62	13.41	12.27	16.29*	14.31*	13.22*	9.54*	7.84	3.08	0.03
1527-318B	–		–	16.82*	14.99*	12.89	9.73	7.3	2.15	-1.2
1541-4EAC	–		–	15.05	13.87	12.8	–		–	–
1633-32F	–		18.52	14.91	12.33	10.32	5.9	4.11	1.51	0.41
1631-598D	–		–	18.25*	16.65*	14.08	12.22	10.75	5.39	2.44
1648-2717	–		–	16.44*	14.88	13.09	11.55	10.45	4.83	0.99
1702-13C	–		–	11.5	9.72	8.99	8.54	8.62	8.68	7.63*
1697-173E	–	17.72	18.69	14.18	13.23	11.98	10.73	9.68	4.09	0.33
1717-203	–		17.4	11.95	10.21	9.23	8.04	7.57	6.83	6.01
1704-2C5	–		–	10.95	10.37	9.89	9.13	8.81	7.78	4.72
1734-1187	16.20	14.87	14.27	14.15	13.12	12.42	11.74	11.39	10.67	8.15
1764-165F	–		–	14.42	13.7	12.57	10.43	9.78	4.66	0.82

^a B , V , and R photometry is from the NOMAD catalog; J , H , and K photometry is from 2MASS; and $W1 - 4$ are from the WISE preliminary source catalog. Questionable magnitudes (due to poor

photometry, blending, contaminants, etc) are marked with an asterisk*.

Table 6. Extinction and Distances for Confirmed WR Stars

Name	Subtype ^a	J^b	H^b	K_s^b	$A_{K_s}^{J-K_s^c}$	$A_{K_s}^{H-K_s^c}$	A_{K_s}	$M_{K_s}^d$	DM	d^e	R_G^e
1040-B6C	WN9	13.134	11.899	11.171	1.32	1.32	1.3	-6.32	16.2	17.2	10.7
1089-1117	cLBV/WNL	16.820	12.595	10.281	4.21	4.38	4.3	-6.32	12.3	2.9	6.0
1093-1765	WN6	15.149	12.925	11.571	2.46	2.40	2.4	-4.94	14.1	6.6	3.6
1139-49EA	WC6::	16.248	–	13.086	–	2.12	–	-4.7	–	–	–
1178-66B	WC9	12.494	11.124	10.259	1.57	1.50	1.5	-4.57	13.3	4.6	4.2
1176-B49	WN9h	12.661	11.218	10.409	1.47	1.51	1.5	-6.34	15.3	11.3	3.6
1198-6EC8	WC6::	–	–	13.467	–	–	–	-4.66	–	–	–
1256-1483A	WN9	–	–	–	–	–	–	-6.32	–	–	–
1319-3BC0	WC7:	14.551	–	12.180	–	1.59	–	-4.84	–	–	–
1338-2B3	WN9	12.608	–	8.790	–	2.56	–	-6.32	–	–	–
1343-284	WN8-9	10.474	9.600	9.018	1.06	0.98	1.0	-5.82	13.8	5.8	2.9
1353-160A	WC8-9	14.108	12.203	11.141	1.93	1.99	2.0	-5.82	15.0	10.0	2.1
1366-438	WN7-8	12.912	–	8.770	–	2.78	–	-5.49	–	–	–
1367-638	WN9	16.152	12.429	10.395	3.70	3.86	3.8	-6.32	12.9	3.9	4.7
1381-19L	WC9	9.663	8.621	8.693	-0.13	0.65	0.3	-4.57	13.0	4.0	7.0
1389-4AB6	WC7	16.131	14.264	12.239	3.69	2.61	3.2	-4.84	13.9	6.1	2.9
1389-1F5D	WN8	–	13.277	11.052	4.05	–	–	-5.82	–	–	–
1446-B1D	WN6	12.210	11.236	10.611	1.14	1.07	1.1	-4.94	14.5	7.8	3.0
1457-673	WC9	14.520	11.444	9.352	3.81	3.46	3.6	-4.57	10.3	1.1	7.5
1485-6C4	WN6	12.035	10.809	10.020	1.44	1.35	1.4	-4.94	13.6	5.2	4.4
1485-844	WN8	14.724	11.299	9.493	3.29	3.50	3.4	-5.82	12.0	2.4	6.4
1495-1D8A	WC8-9	–	–	11.716	–	–	–	-5.04	–	–	–
1495-705	WN8	14.971	11.381	9.164	4.03	3.89	4.0	-5.82	11.0	1.6	7.1
1514-AA0	WC8	12.921	11.244	10.537	1.29	1.60	1.4	-5.04	14.1	6.7	4.2
1509-2E64	WC9	–	–	12.446	–	–	–	-4.57	–	–	–
1525-2352	WC8:	–	14.748	12.444	4.19	–	–	-5.04	–	–	–
1519-E43	WC7	–	13.039	11.262	3.23	–	–	-4.84	–	–	–
1530-8FA	WN5	12.759	11.425	10.642	1.43	1.42	1.4	-3.86	13.1	4.1	5.4
1541-3C8	WC8	–	13.856	12.154	3.10	–	–	-5.04	–	–	–
1541-197C	WC8	15.144	13.280	11.617	3.03	2.36	2.7	-5.04	14.0	6.2	4.7
1544-FA4	WN5	13.741	12.240	10.827	2.57	1.95	2.3	-3.86	12.4	3.1	6.2
1547-1DF2	WN8:	14.195	12.504	11.756	1.36	1.63	1.5	-5.82	16.1	16.4	10.4
1553-9E8	WN9h	15.760	12.864	10.976	3.44	3.21	3.3	-6.34	14.0	6.3	4.8
1547-1488	WN5	13.956	12.254	11.159	1.99	1.87	1.9	-3.86	13.1	4.1	5.5
1553-15DF	WC8	–	14.803	12.065	4.98	–	–	-5.04	–	–	–
1602-9AF	WN6	13.109	11.619	11.050	1.04	1.38	1.2	-4.94	14.8	9.1	6.1

REFERENCES

- Acker, A., Marcout, J., Ochsenbein, F., Stenholm, B., Tytenda, R., & Schohn, C. 1992, The Strasbourg-ESO Catalogue of Galactic Planetary Nebulae. Parts I, II.
- Chaves, R. C. G. & for the H. E. S. S Collaboration. 2009, arXiv, astro-ph.HE
- Cherepashchuk, A. M. & Postnov, K. A. 2000, eprint arXiv, 12512
- Conti, P. S. 1976, (Ministere de l'Education National, 9, 193
- Crowther, P. A. 2007, Annual Review of Astronomy & Astrophysics, 45, 177
- Crowther, P. A., Hadfield, L. J., Clark, J. S., Negueruela, I., & Vacca, W. D. 2006a, MNRAS, 372, 1407
- Crowther, P. A., Morris, P. W., & Smith, J. D. 2006b, ApJ, 636, 1033
- Cushing, M. C., Vacca, W. D., & Rayner, J. T. 2004, PASP, 116, 362
- Detmers, R. G., Langer, N., Podsiadlowski, P., & Izzard, R. G. 2008, Astronomy and Astrophysics, 484, 831
- Evans, I. N., Primini, F. A., Glotfelty, K. J., Anderson, C. S., Bonaventura, N. R., Chen, J. C., Davis, J. E., Doe, S. M., Evans, J. D., Fabbiano, G., Galle, E. C., Gibbs, D. G., Grier, J. D., Hain, R. M., Hall, D. M., Harbo, P. N., He, X. H., Houck, J. C., Karovska, M., Kashyap, V. L., Lauer, J., McCollough, M. L., McDowell, J. C., Miller, J. B., Mitschang, A. W., Morgan, D. L., Mossman, A. E., Nichols, J. S., Nowak, M. A., Plummer, D. A., Refsdal, B. L., Rots, A. H., Siemiginowska, A., Sundheim, B. A., Tibbetts, M. S., Stone, D. W. V., Winkelman, S. L., & Zografou, P. 2010, The Astrophysical Journal Supplement, 189, 37
- Faherty, J. K., Shara, M. M., Zurek, D., Kanarek, G., & Moffat, A. F. J. 2014, AJ, 147, 115
- Figer, D. F., McLean, I. S., & Najarro, F. 1997, Astrophysical Journal v.486, 486, 420
- Greene, T. P. & Lada, C. J. 1996, AJ, 112, 2184
- Guerrero, M. A. & Chu, Y.-H. 2008, ApJS, 177, 216
- Gvaramadze, V. V., Kniazev, A. Y., & Fabrika, S. 2010, MNRAS, 405, 1047
- Hadfield, L. J., van Dyk, S. D., Morris, P. W., Smith, J. D., Marston, A. P., & Peterson, D. E. 2007, MNRAS, 376, 248
- Indebetouw, R., Mathis, J. S., Babler, B. L., Meade, M. R., Watson, C., Whitney, B. A., Wolff, M. J., Wolfire, M. G., Cohen, M., Bania, T. M., Benjamin, R. A., Clemens, D. P., Dickey, J. M., Jackson, J. M., Kobulnicky, H. A., Marston, A. P., Mercer, E. P., & Stauffer, J. R. 2005, The Astrophysical . . . , 931

Table 6—Continued

Name	Subtype ^a	J^b	H^b	K_s^b	$A_{K_s}^{J-K_s^c}$	$A_{K_s}^{H-K_s^c}$	A_{K_s}	$M_{K_s}^d$	DM	d^e	R_G^e
1603-11AD	WN5	16.131	13.635	12.156	2.69	2.66	2.7	-3.86	13.3	4.7	5.8
1609-1C95	WC9	–	15.069	11.927	5.72	–	–	-4.57	–	–	–
1626-4FC8	[WC6:]	15.593	14.858	13.885	1.77	1.14	1.5	–	–	–	–
1629-14D6	WN9h	14.727	13.441	12.625	1.49	1.41	1.5	-6.34	17.5	31.9	26.4
1627-A6D	WC7::	15.853	13.537	11.753	3.25	2.75	3.0	-4.84	13.6	5.2	5.9
1635-AD8	WN6	15.201	12.874	11.478	2.54	2.49	2.5	-4.94	13.9	6.0	5.9
1653-FFE	WN5-6	15.150	–	11.658	–	2.34	–	-3.86	–	–	–
1651-BB4	WN5	15.825	–	11.730	–	2.74	–	-3.86	–	–	–
1647-1E70	WC8:	–	15.095	12.565	4.60	–	–	-5.04	–	–	–
1659-212	WN9	13.436	10.891	9.527	2.48	2.62	2.6	-6.32	13.3	4.6	6.3
1669-3DF	WN9h	12.788	11.035	9.966	1.95	1.89	1.9	-6.34	14.4	7.5	6.6
1660-1169	WC6:	14.652	13.293	12.076	2.21	1.73	2.0	-4.66	14.8	9.0	7.0
1697-38F	WC9	12.966	11.176	9.922	2.28	2.04	2.2	-4.57	12.3	2.9	7.1
1702-23L	WC8	11.860	10.996	10.205	1.44	1.11	1.3	-5.04	14.0	6.2	6.8
1695-2B7	WC9	13.012	11.089	9.641	2.64	2.26	2.5	-4.57	11.8	2.3	7.3

^aIt is difficult to differentiate between features of WC4 – 8. A colon (:) indicates an uncertainty of up to ± 2 subtypes.

^bIn cases where 2MASS J and K_s magnitudes were unreliable (as described in table 4), J and $CONT2$ magnitudes, respectively, from the Shara et al. survey were used instead, when available. These magnitudes were scaled to match 2MASS values in the reduction process.

^c K -band extinction was calculated from 2MASS colors and subtype values provided in Crowther et al. (2006a).

^d M_{K_s} values are derived for spectral subtypes by Paul Crowther (via private communication).

^eDistances (d) and Galactocentric radii (R_G) are in kpc, with typical uncertainties of $\sim 25\%$.

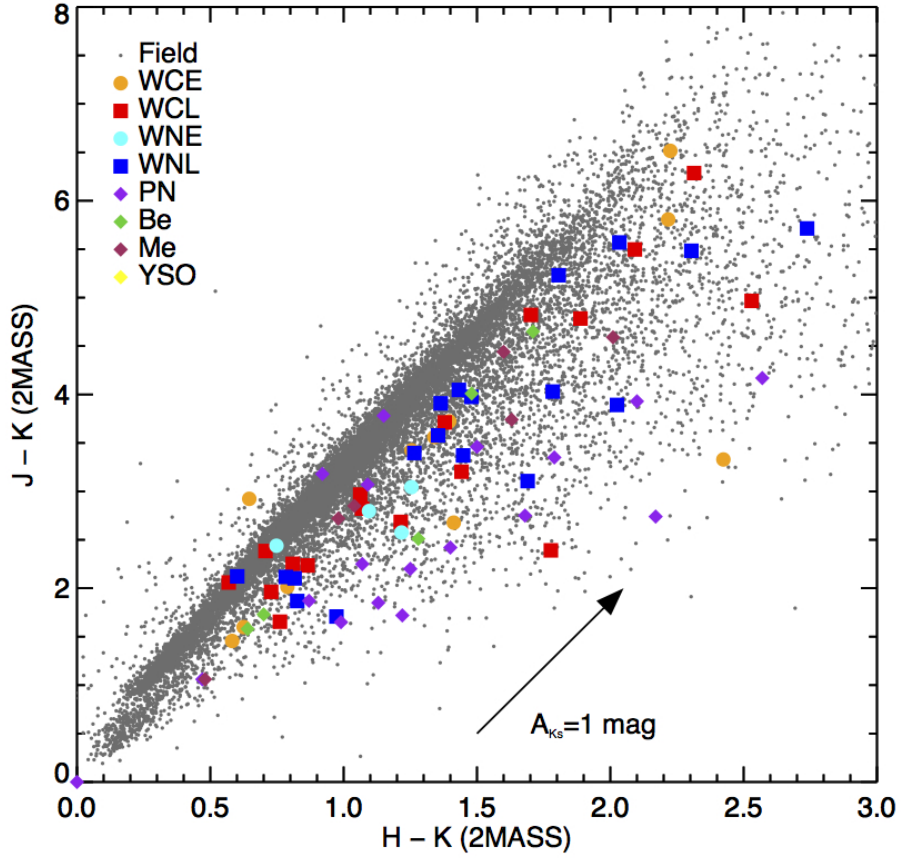


Fig. 5.— A color-color plot like that in figure 4 - Top, displaying the NIR colors for the new emission-line objects classified in this work. Grey dots are field stars; orange and cyan circles are early-type WCs and WNs respectively, while red and blue squares are late-type WCs and WNs. Purple diamonds are PNe, green diamonds are Be stars, brown diamonds are emitting M-giants and supergiants, and yellow diamonds are probable YSOs. The reddening vector is as in figure 4.

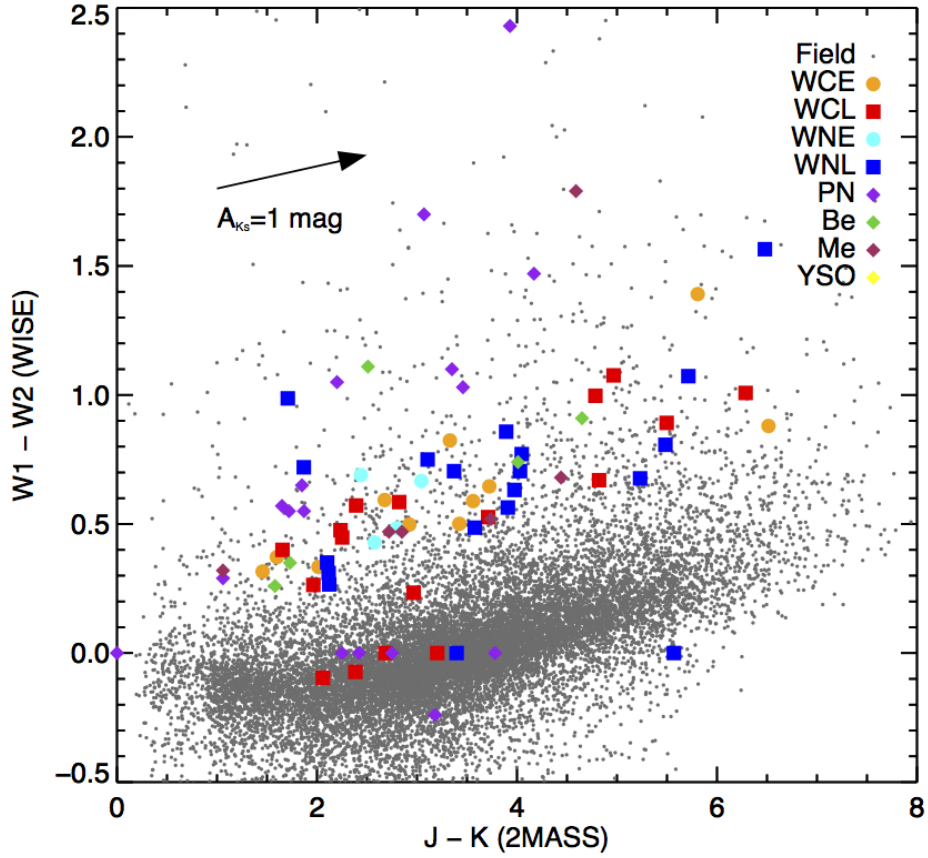


Fig. 6.— A color-color plot like that in figure 4, displaying the NIR and MIR colors for the new emission-line objects classified in this work. Symbols and colors as in figure 5. Three new WR stars are below the cut line; these have extremely close neighbors which lie on the same WISE pixel and confuse the magnitudes. The reddening vector is as in figure 4.

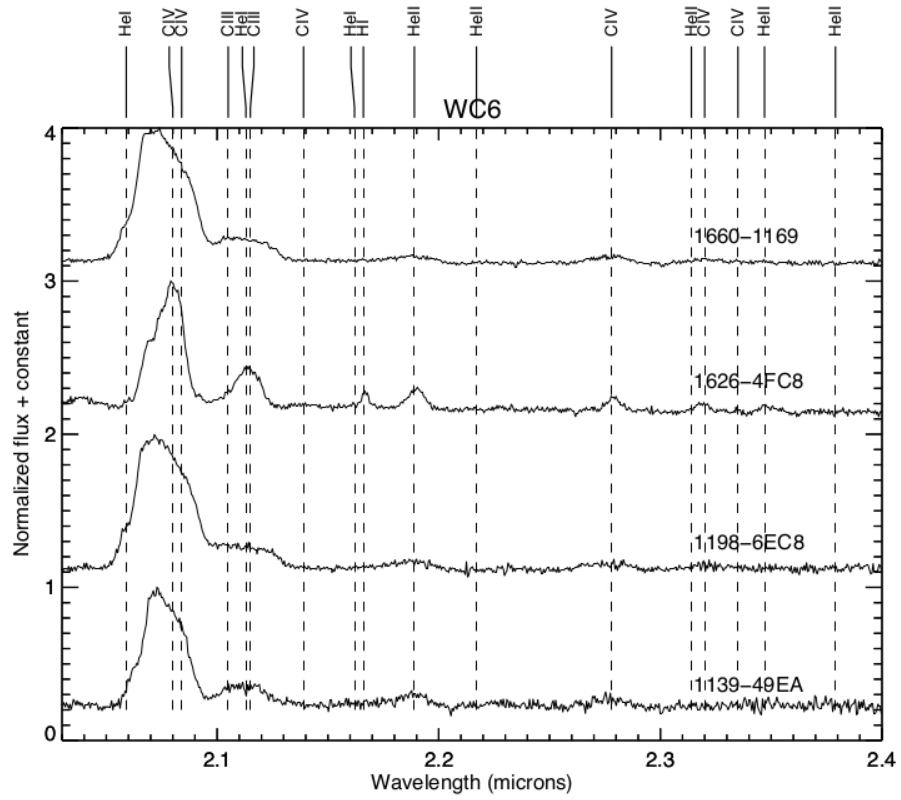


Fig. 7.— All new WC6 objects classified in this work, showing the characteristic extremely strong C IV lines.

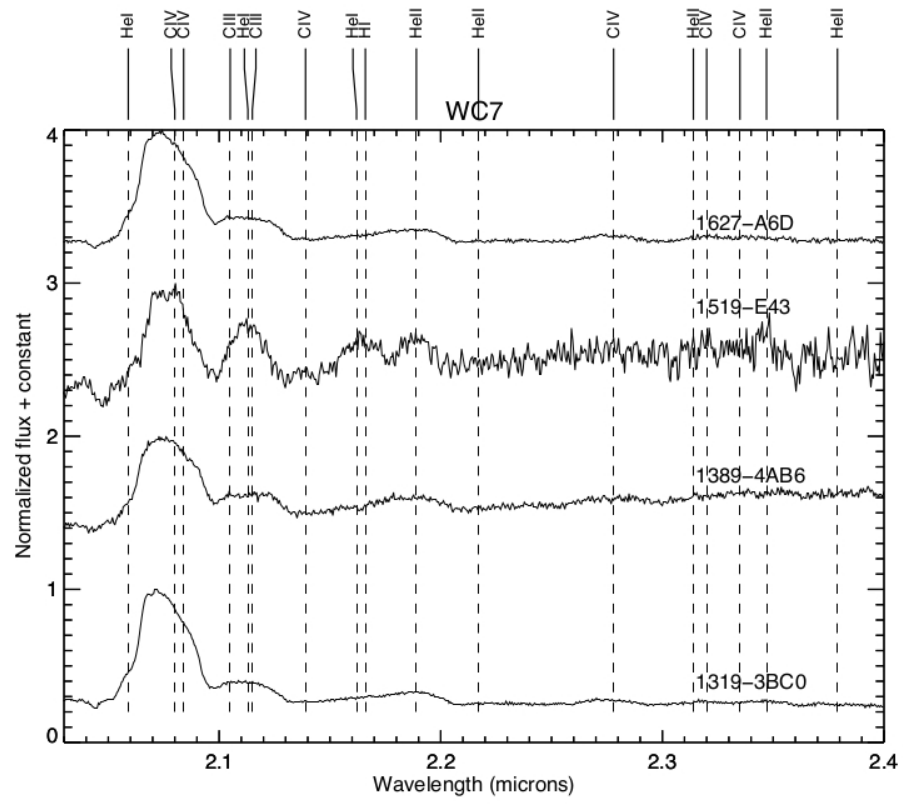


Fig. 8.— All new WC7 objects classified in this work.

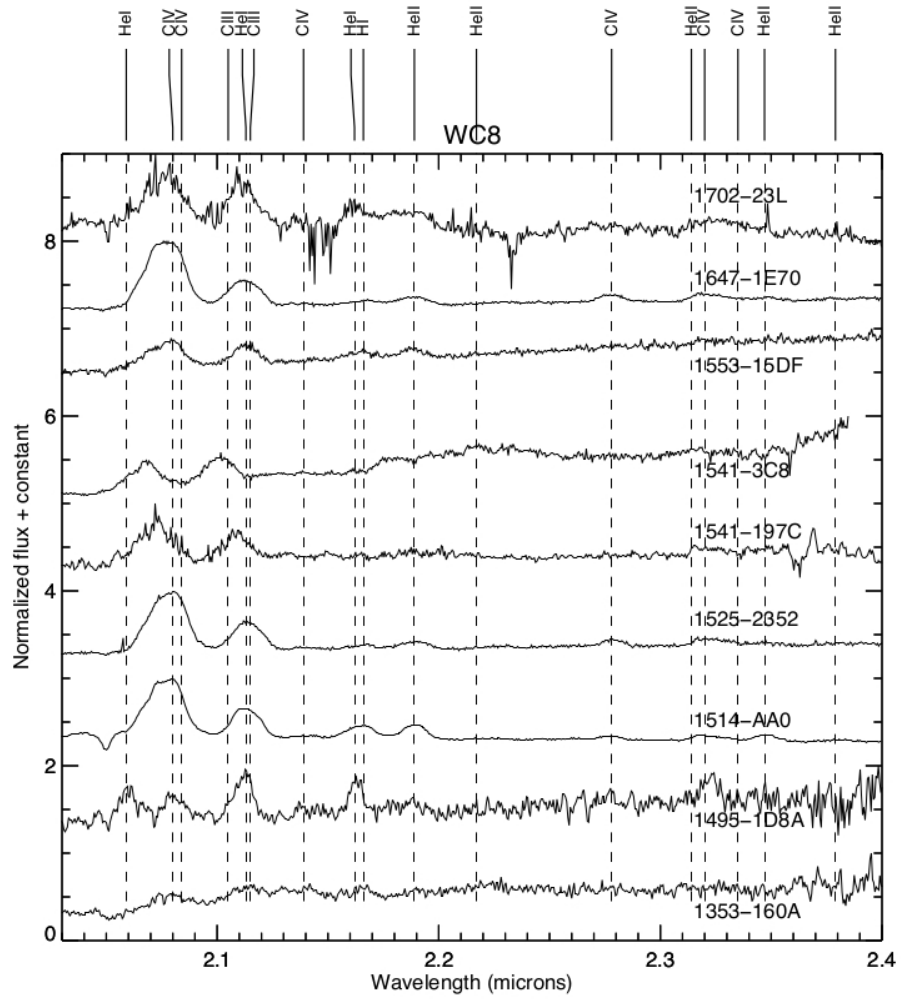


Fig. 9.— All new WC8 objects classified in this work.

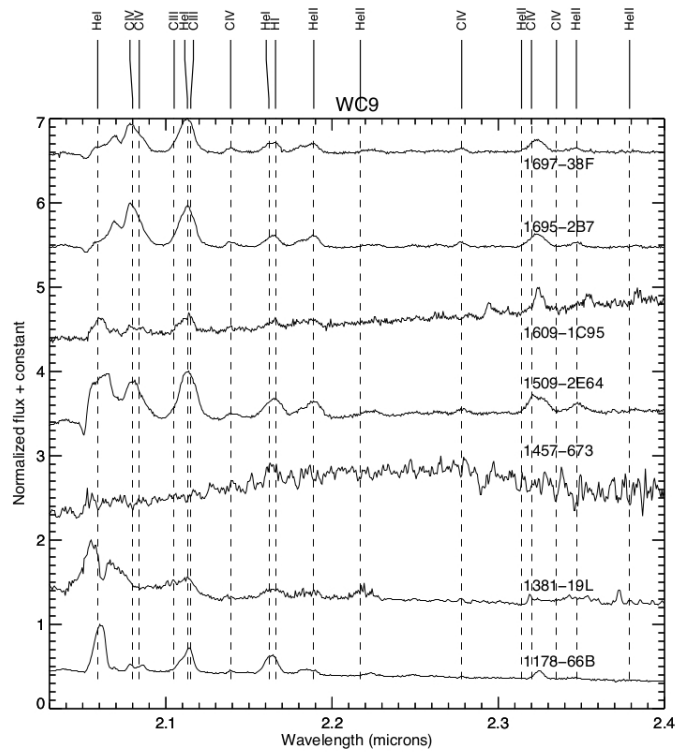


Fig. 10.— All new WC9 objects classified in this work.

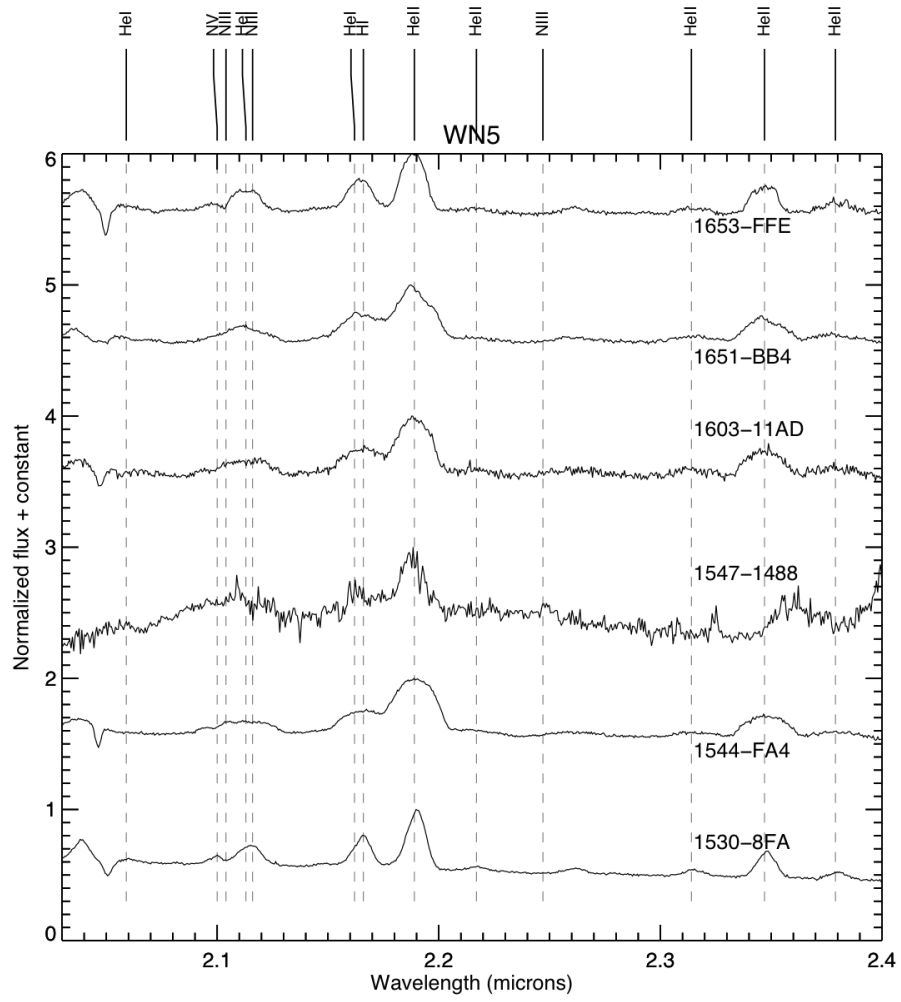


Fig. 11.— All new WN5 objects classified in this work.

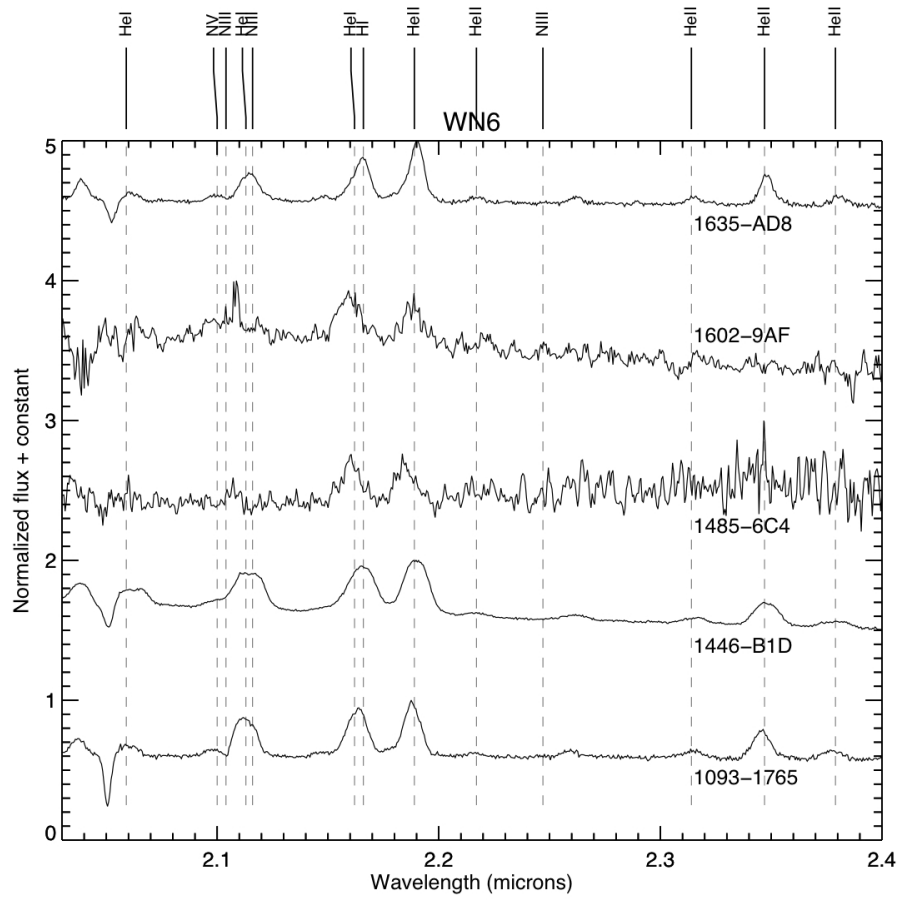


Fig. 12.— All new WN6 objects classified in this work.

- Kerber, F., Mignani, R. P., Guglielmetti, F., & Wicenec, A. 2003, *A&A*, 408, 1029
- Langon, A., Hauschildt, P. H., Ladjal, D., & Mouhcine, M. 2007, *A&A*, 468, 205
- Langon, A. & Wood, P. R. 2000, *A&AS*, 146, 217
- Landsman, W. B. 1993, *Astronomical Data Analysis Software and Systems II*, 52, 246
- Lang, D., Hogg, D. W., Mierle, K., Blanton, M., & Roweis, S. 2010, *The Astronomical Journal*, 139, 1782
- Lépine, S. & Moffat, A. F. J. 1999, *The Astrophysical Journal*, 514, 909
- Mauerhan, J. C., Munro, M. P., Morris, M. R., Stolovy, S. R., & Cotera, A. 2010, *ApJ*, 710, 706
- Mauerhan, J. C., Van Dyk, S. D., & Morris, P. W. 2011, *AJ*, 142, 40
- Miszalski, B., Parker, Q. A., Acker, A., Birkby, J. L., Frew, D. J., & Kovacevic, A. 2008, *MNRAS*, 384, 525
- Predehl, P. & Schmitt, J. H. M. M. 1995, *A&A*, 293, 889
- Rayner, J. T., Cushing, M. C., & Vacca, W. D. 2009, *ApJS*, 185, 289
- Rieke, G. H. & Lebofsky, M. J. 1985, *ApJ*, 288, 618
- Rosslowe, C. K. & Crowther, P. A. 2013, in *Massive Stars: From alpha to Omega*
- Shara, M. M., Faherty, J. K., Zurek, D., Moffat, A. F. J., Gerke, J., Doyon, R., Artigau, E., & Drissen, L. 2012, *AJ*, 143, 149
- Shara, M. M., Moffat, A. F. J., Gerke, J., Zurek, D., Stanonik, K., Doyon, R., Artigau, E., Drissen, L., & Villar-Sbaffi, A. 2009, *The Astronomical Journal*, 138, 402
- Shara, M. M., Moffat, A. F. J., Smith, L. F., Niemela, V. S., Potter, M., & Lamontagne, R. 1999, *AJ*, 118, 390
- Skinner, S., Güdel, M., Schmutz, W., & Zhekov, S. 2006, *Ap&SS*, 304, 97
- Skrutskie, M. F., Cutri, R. M., Stiening, R., Weinberg, M. D., Schneider, S., Carpenter, J. M., Beichman, C., Capps, R., Chester, T., Elias, J., Huchra, J., Liebert, J., Lonsdale, C., Monet, D. G., Price, S., Seitzer, P., Jarrett, T., Kirkpatrick, J. D., Gizis, J. E., Howard, E., Evans, T., Fowler, J., Fullmer, L., Hurt, R., Light, R., Kopan, E. L., Marsh, K. A., McCallon, H. L., Tam, R., Dyk, S. V., & Wheelock, S. 2006, *The Astronomical Journal*, 131, 1163
- Smith, J. D. T., Cushing, M., Barletta, A., McCarthy, D., Kulesa, C., & Van Dyk, S. D. 2012, *AJ*, 144, 166

- Stetson, P. B. 1987, *Astronomical Society of the Pacific*, 99, 191
- . 1994, *Publications of the Astronomical Society of the Pacific*, 106, 250
- Stringfellow, G. S., Gvaramadze, V. V., Beletsky, Y., & Kniazev, A. Y. 2012, in *IAU Symposium*, Vol. 282, *IAU Symposium*, ed. M. T. Richards & I. Hubeny, 267–268
- Urquhart, J. S., Hoare, M. G., Purcell, C. R., Lumsden, S. L., Oudmaijer, R. D., Moore, T. J. T., Busfield, A. L., Mottram, J. C., & Davies, B. 2009, *A&A*, 501, 539
- Vacca, W. D., Cushing, M. C., & Rayner, J. T. 2004, *PASP*, 116, 352
- van der Hucht, K. A. 2001, *VizieR Online Data Catalog*, 3215, 0
- van der Hucht, K. A. 2006, *Astronomy and Astrophysics*, 458, 453
- Wachter, S., Mauerhan, J., van Dyk, S., Hoard, D. W., & Morris, P. 2011, *Bulletin de la Societe Royale des Sciences de Liege*, 80, 291
- Wolf, C. J. E. & Rayet, G. 1867, *Comptes Rendus*, 65, 292
- Woosley, S. & Bloom, J. 2006, *Annual Review of Astronomy and Astrophysics*, 44, 507
- Wright, E. L., Eisenhardt, P. R. M., Mainzer, A. K., Ressler, M. E., Cutri, R. M., Jarrett, T., Kirkpatrick, J. D., Padgett, D., McMillan, R. S., Skrutskie, M., Stanford, S. A., Cohen, M., Walker, R. G., Mather, J. C., Leisawitz, D., Gautier, III, T. N., McLean, I., Benford, D., Lonsdale, C. J., Blain, A., Mendez, B., Irace, W. R., Duval, V., Liu, F., Royer, D., Heinrichsen, I., Howard, J., Shannon, M., Kendall, M., Walsh, A. L., Larsen, M., Cardon, J. G., Schick, S., Schwalm, M., Abid, M., Fabinsky, B., Naes, L., & Tsai, C.-W. 2010, *AJ*, 140, 1868

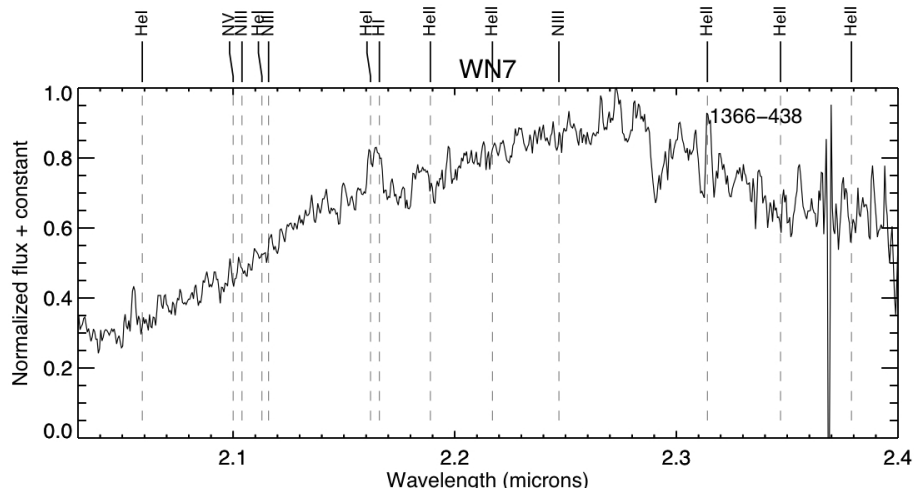


Fig. 13.— Top: All new WN7 objects classified in this work.

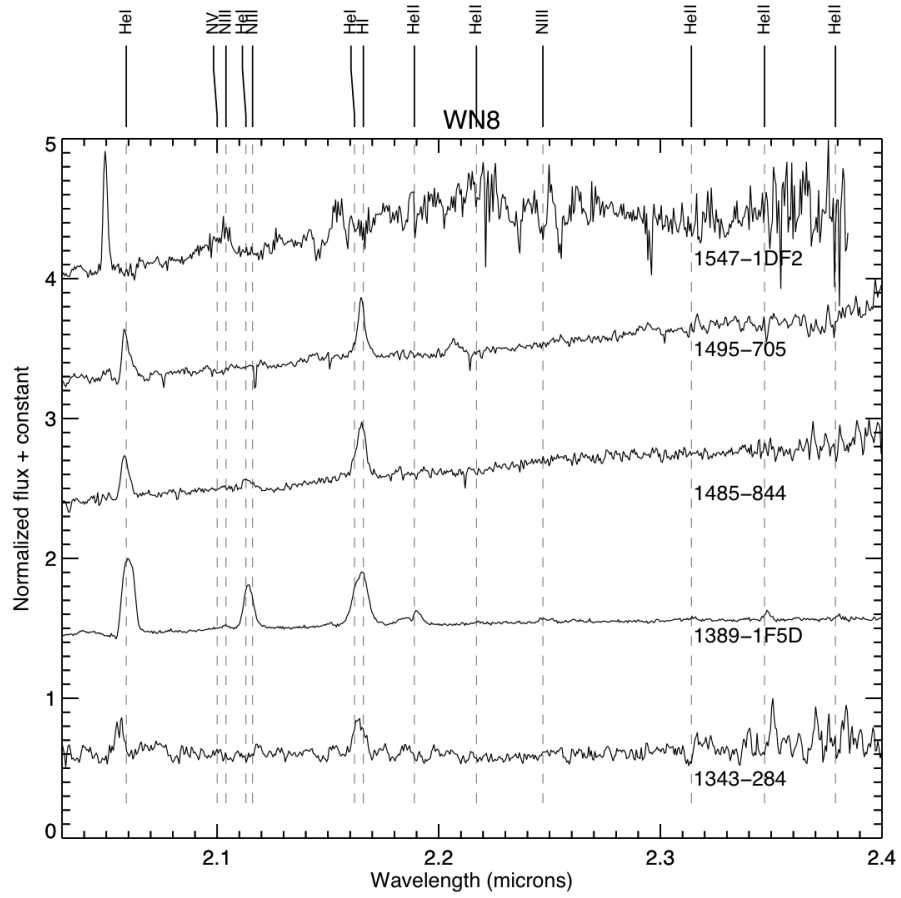


Fig. 14.— All new WN8 objects classified in this work.

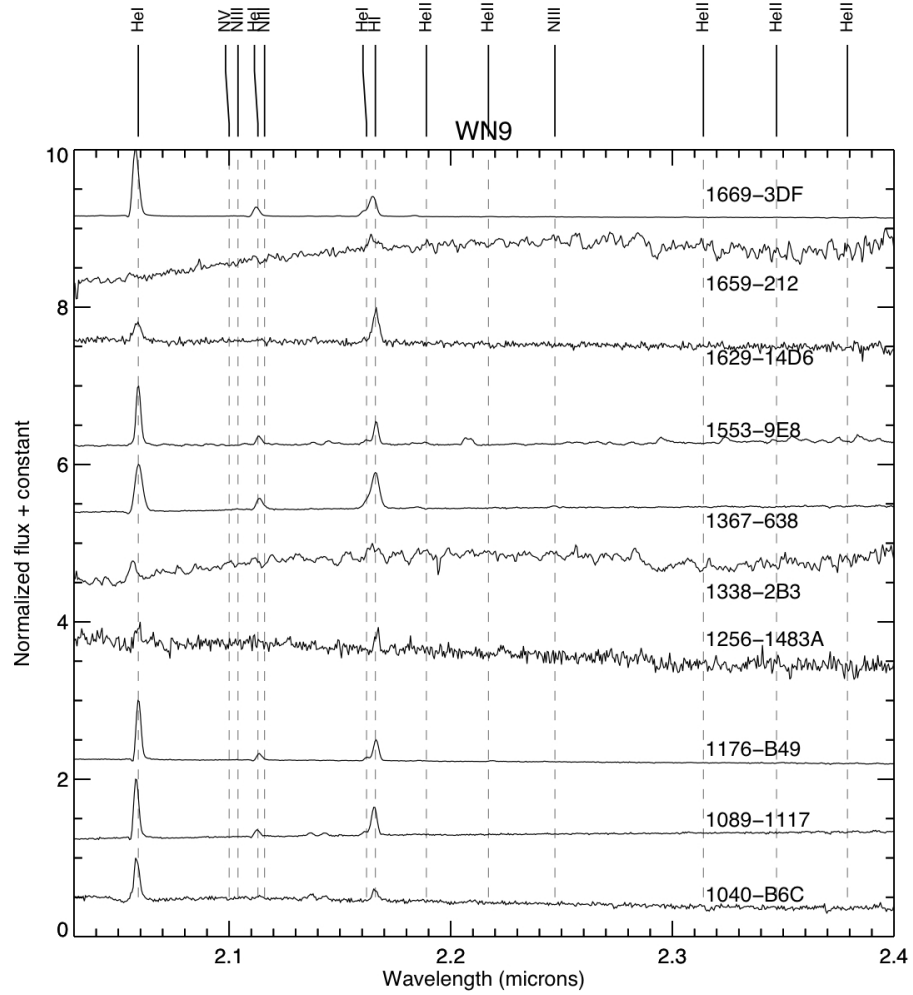


Fig. 15.— All new WN9 objects classified in this work. Object 1089-1117 (cLBV transitioning to WNL) is included, as the spectral lines are similar to those of a WN9.

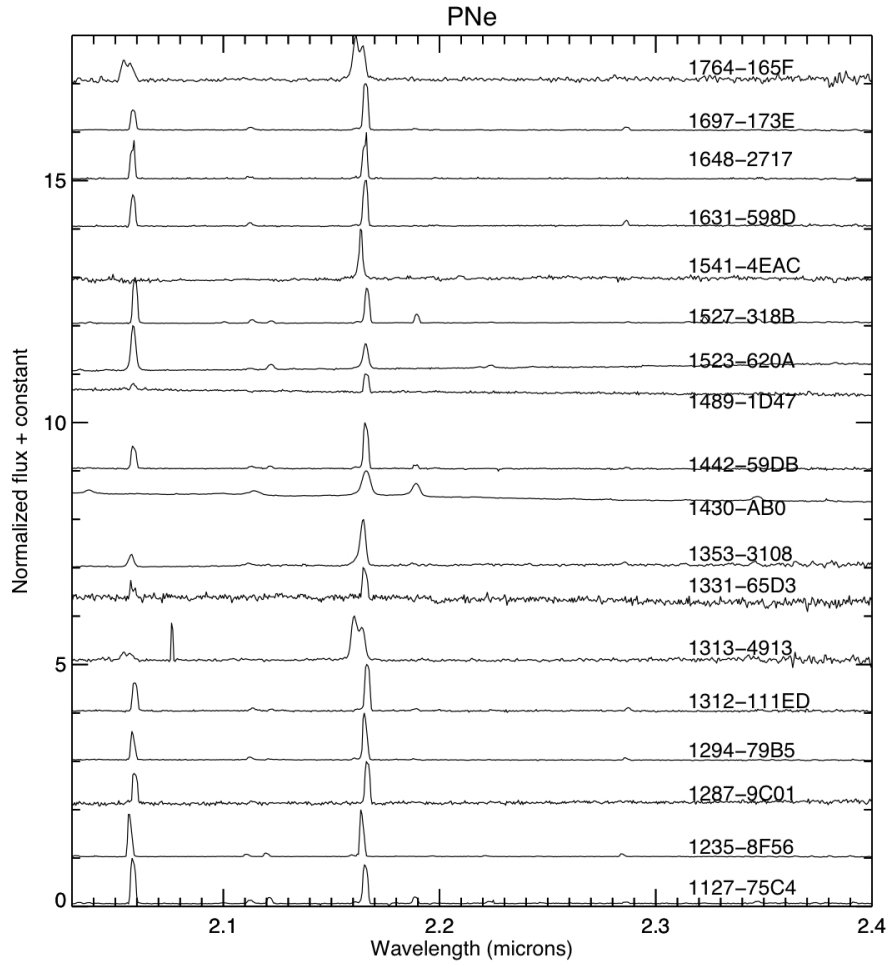


Fig. 16.— All new PNe classified in this work. Note the doubled emission lines for 3 of the PN spectra. The selection criteria used to identify strong Wolf-Rayet candidates are also extremely effective at identifying new PNe; the search for new PNe is described in a paper in preparation.



Fig. 17.— Likely YSOs, as these spectra lack the CO bands redwards of $2.3\mu\text{m}$ which identify emitting red giants and supergiants.

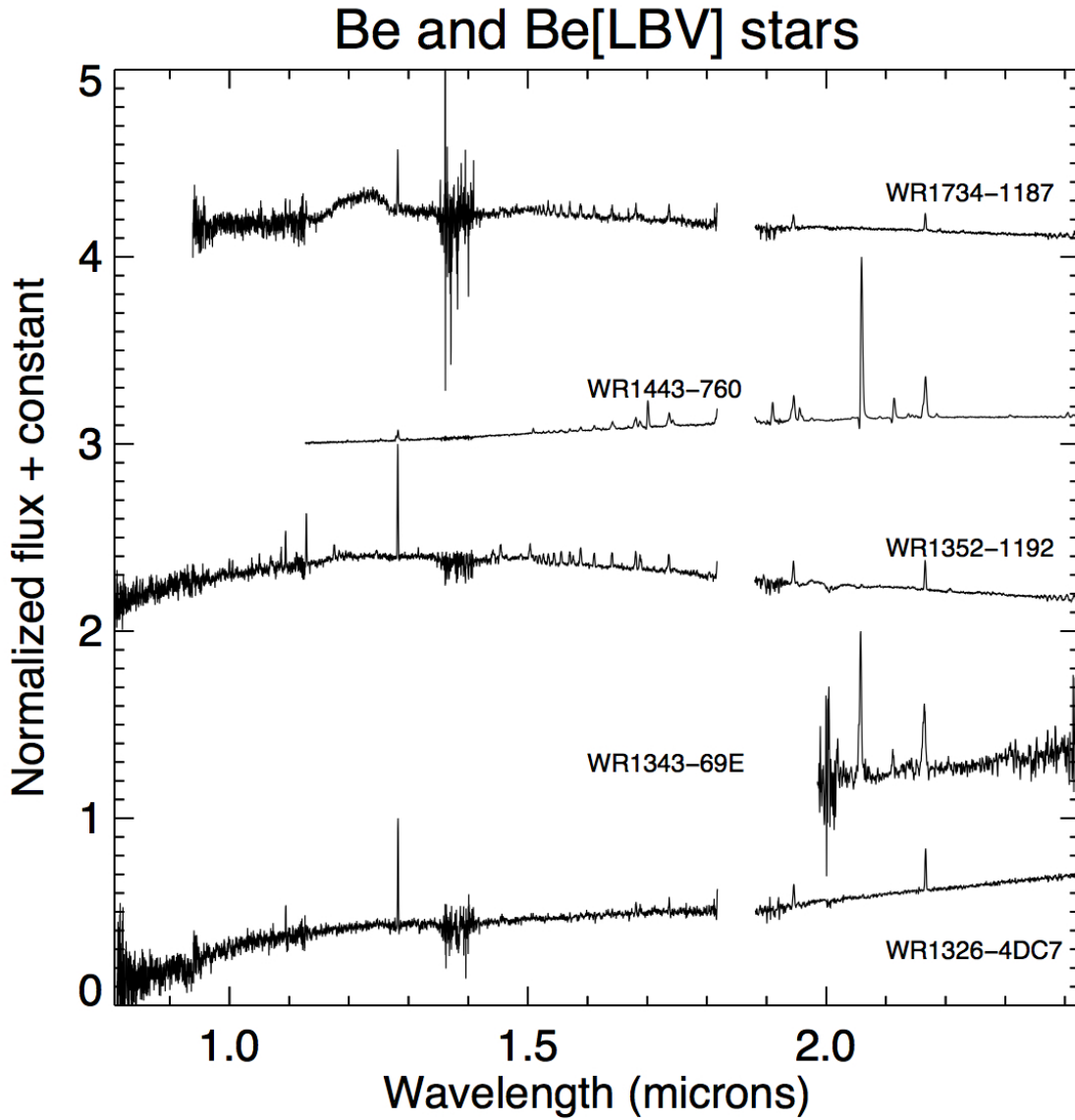


Fig. 18.— All new Be stars classified in this work. The full JHK spectrum is shown for these objects, displaying the prominent Brackett series for those spectra for which we have J and H spectra. Be star interlopers are relatively common, as they are selected strongly by the BrGamma filter and can only be ruled out by obtaining spectra.

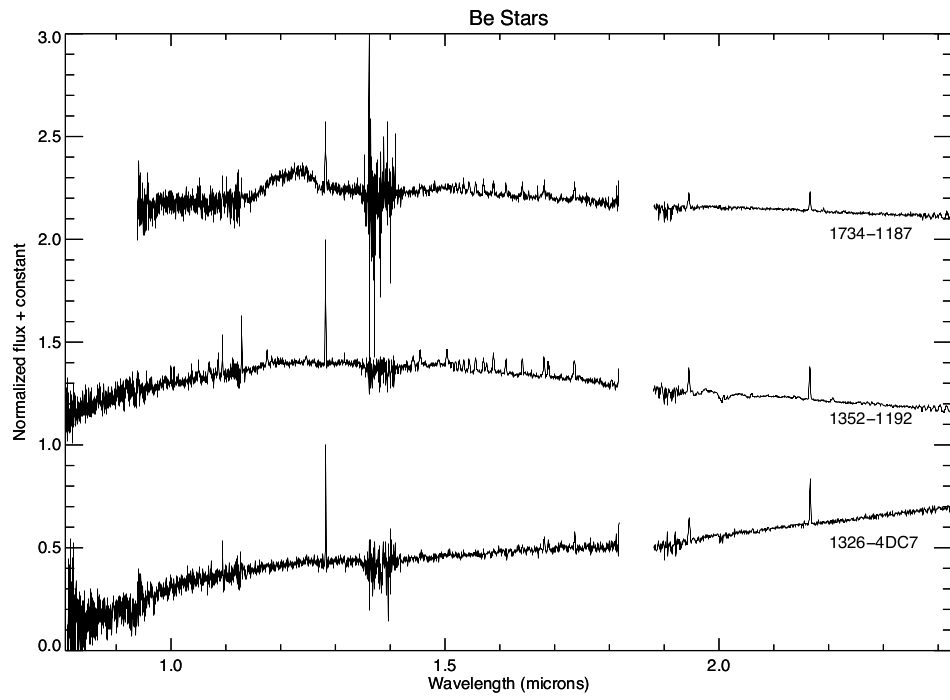


Fig. 19.— Red giants or supergiants, with molecular CO bands redwards of $2.3\mu\text{m}$, which showed HI emission.

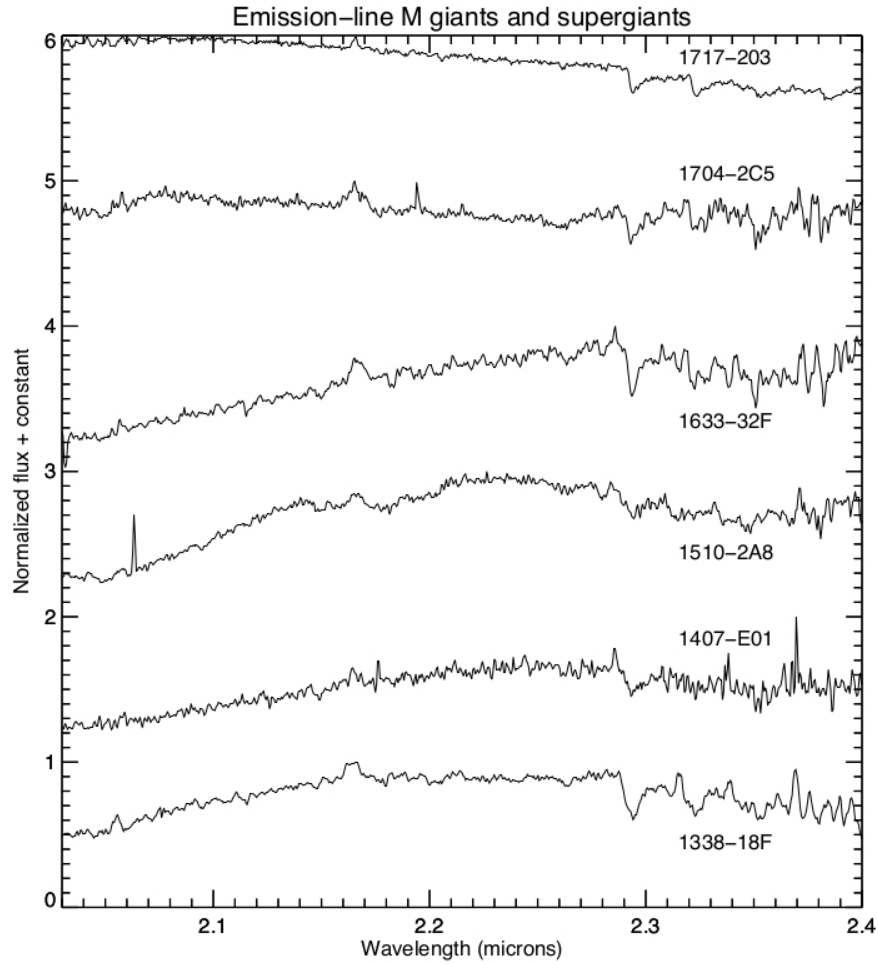


Fig. 20.— A selection of non-emitting red giants or supergiants. These interlopers are selected simply because the slope of the red spectrum makes them brighter in C IV than in He I or the nearest continuum filter.

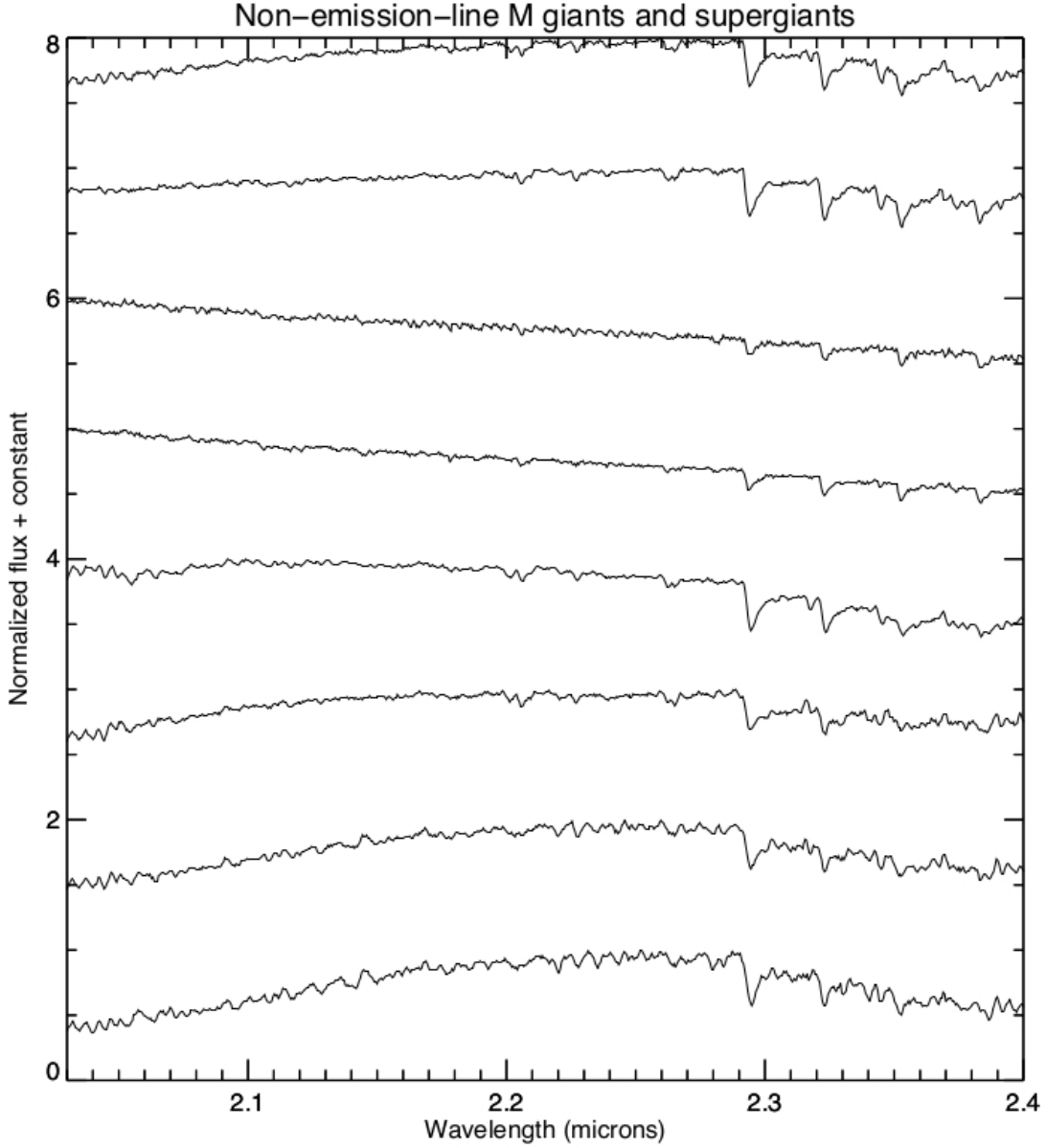


Fig. 21.— Top: A histogram of WR stars per 5° of longitude, with those WRs lying within the survey bounds overplotted in cyan. 80% of all current WR stars lie within the bounds of the survey. The histogram shows clear spikes where the telescope looks along the Milky Way’s spiral arms, as predicted by simulations presented in the appendix of Paper I. Bottom: The distribution of WR stars projected on the sky, as a function of Galactic latitude and longitude. Blue circles (WN) and red squares (WC) are WR stars from the literature, while green circles (WN) and orange squares (WC) indicate the contribution by this survey, as detailed in Papers I, II, and this work. The cyan box shows the survey extent; the great majority of WR stars in the Galaxy lie in the Galactic plane, within 60-90 degrees of the Galactic center.

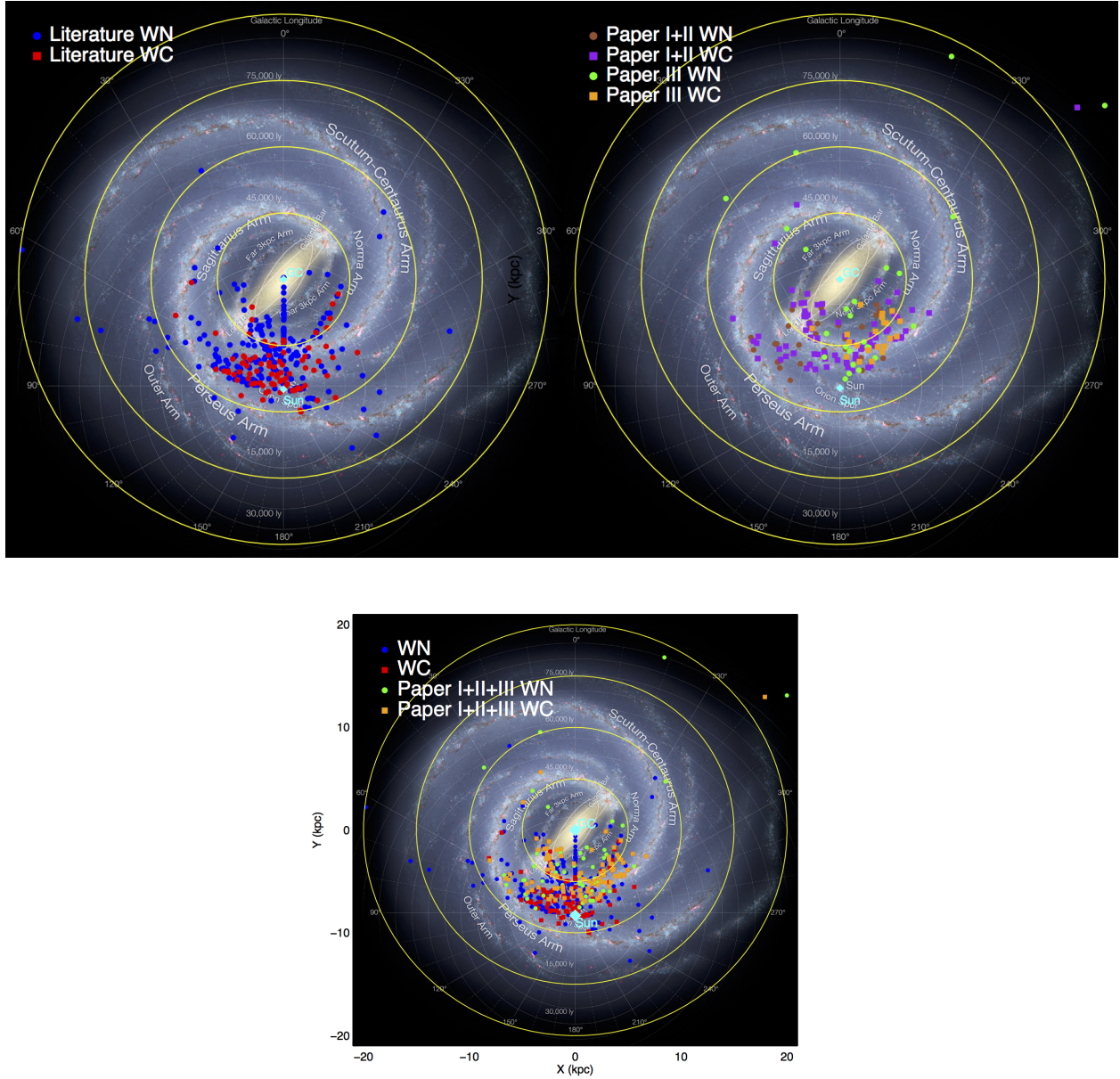


Fig. 22.— The distribution of confirmed WR stars projected onto the plane of the Galaxy, superimposed over an artist’s representation of the Milky Way (image credit: NASA/JPL-Caltech/ESO/R. Hurt). Top shows WRs from the literature only (left), and from Papers I, II, and this paper (right), highlights the different regions of the Galaxy probed by the Shara et al. survey; in particular, note that the Shara survey has more than doubled the number of confirmed WR stars on the far side of the Galaxy. All confirmed Galactic WR stars are shown in the bottom plot, where the distribution can clearly be seen to trace out the spiral arms on the near side of the Galaxy. Thus, as new WRs are identified on the far side, we can use that growing population as tracers of recent massive star formation, and infer a map of the spiral arms on the Galactic far side.

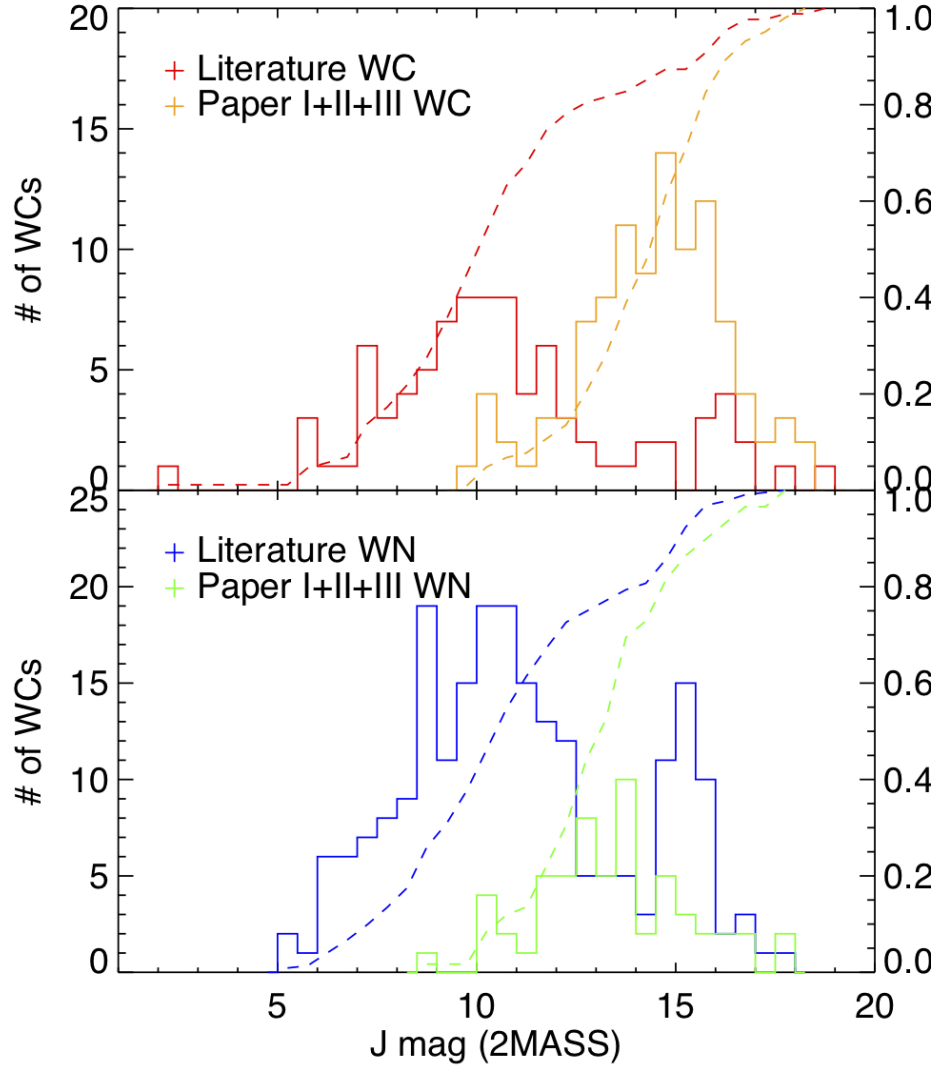


Fig. 23.— Histogram of J-band 2MASS magnitudes for WN and WC stars, identified in the literature or from the Shara et al. survey. Also shown is the cumulative fraction identified, as a function of J magnitude. The survey detailed in Papers I and II and in this paper has contributed WR stars in regions of magnitude-space which are poorly probed by the literature; the survey has identified far more faint WCs in particular than other surveys.

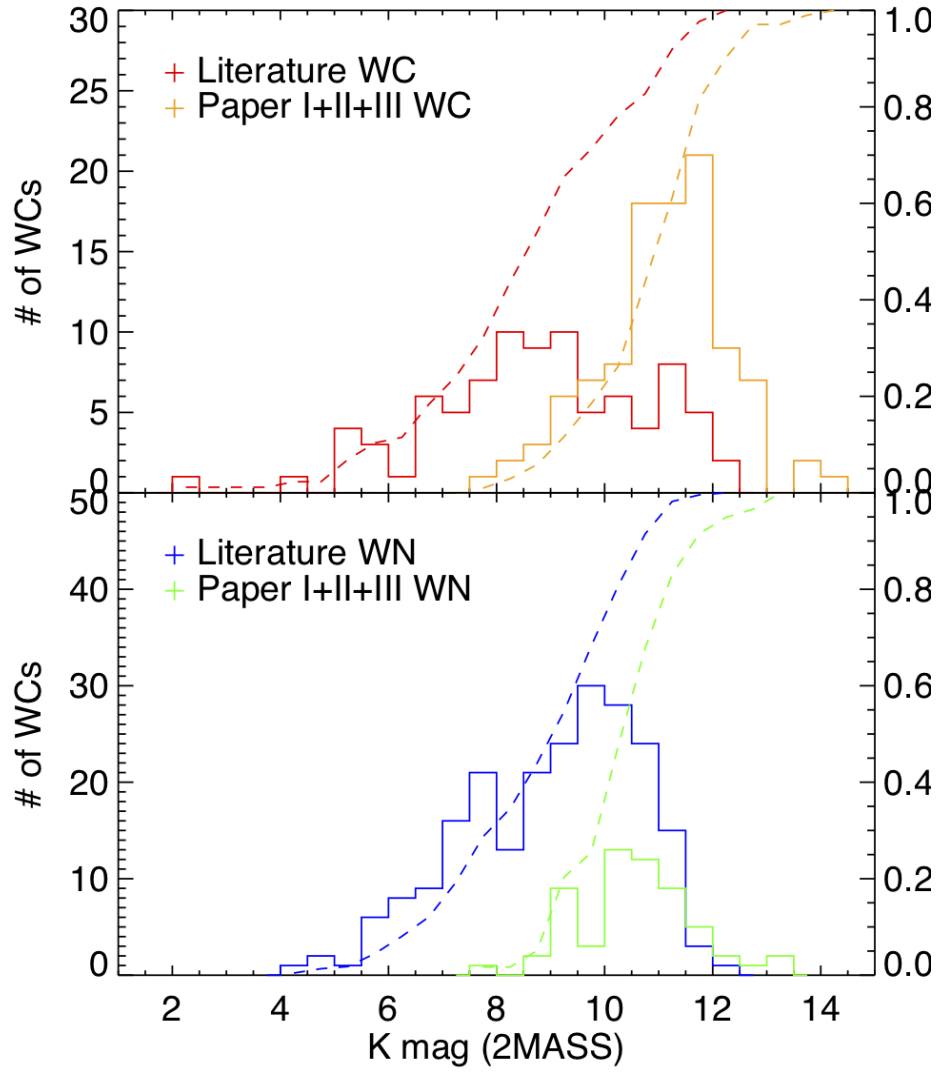


Fig. 24.— As figure 23, but for K magnitudes. Once again, it is readily apparent that the Shara et al. survey is extremely useful for identifying faint WC stars.

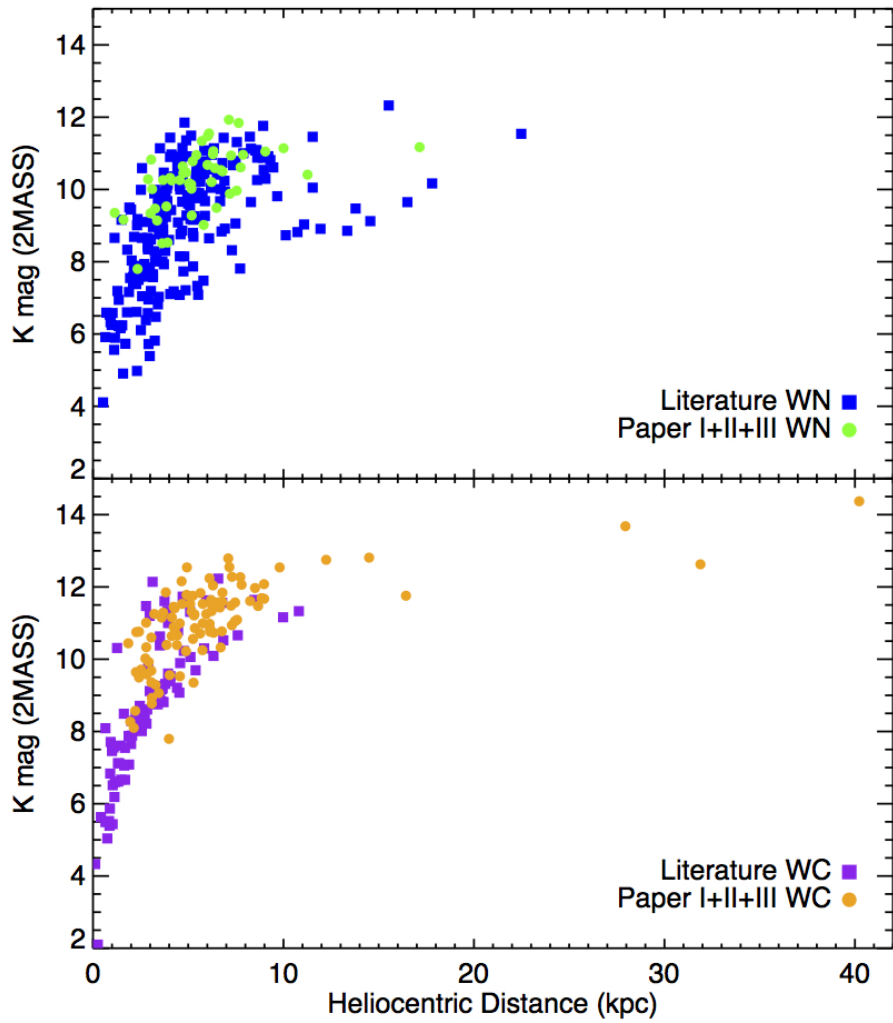


Fig. 25.— K-band magnitude (2MASS) as a function of heliocentric distance for WCs and WNs. The Shara et al. survey has identified the most distant and the faintest WNs and (especially) WCs in the Milky Way.

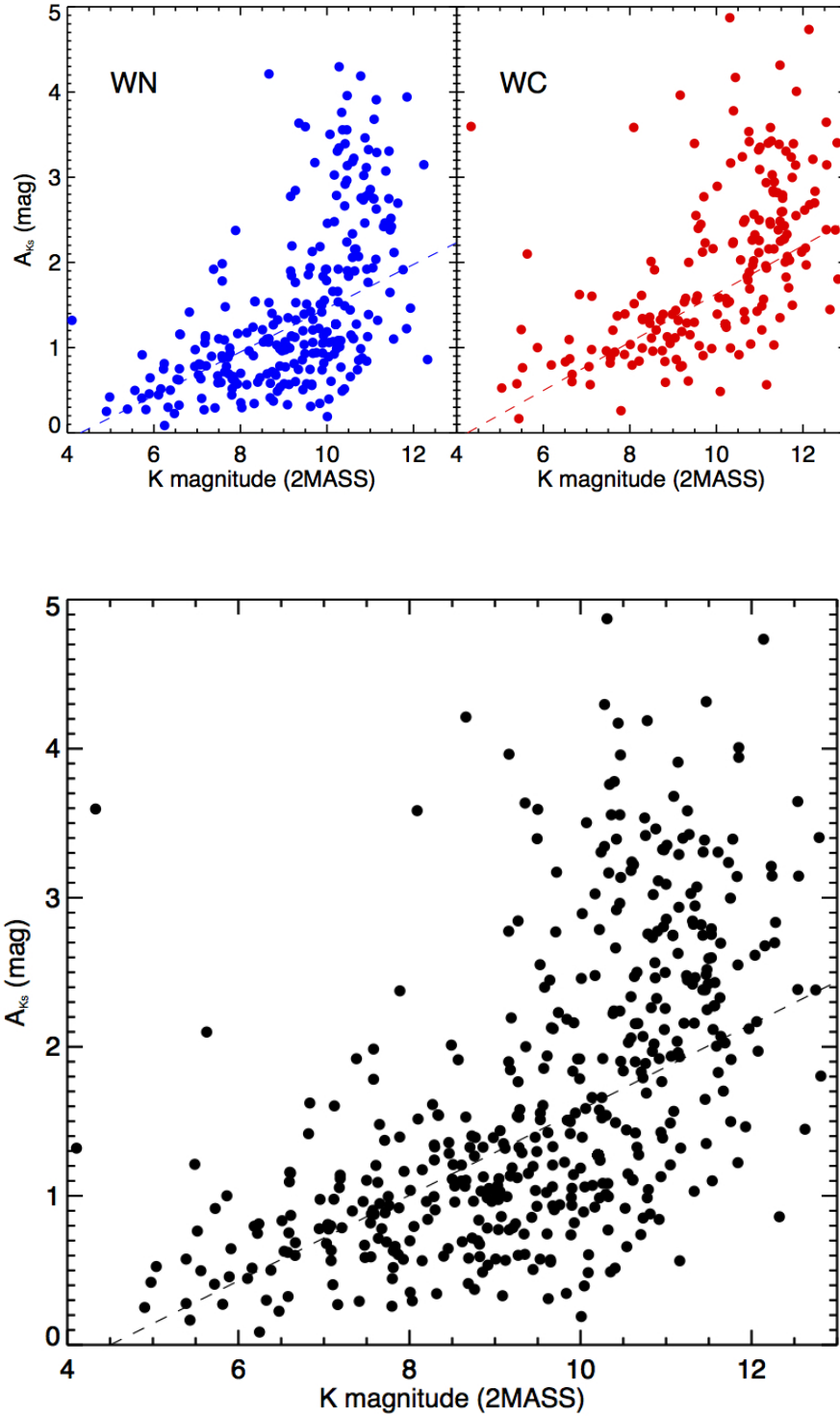


Fig. 26.— K-band absorption vs magnitude, using 2MASS magnitudes of WR stars from this paper and the literature. Top left shows WNs only, top right shows WCs, and bottom shows the total population. In each case a Least-Absolute-Deviation fit to the points has been included, showing the expected trend of greater extinction for fainter (and therefore more distant) Wolf-Rayet stars.

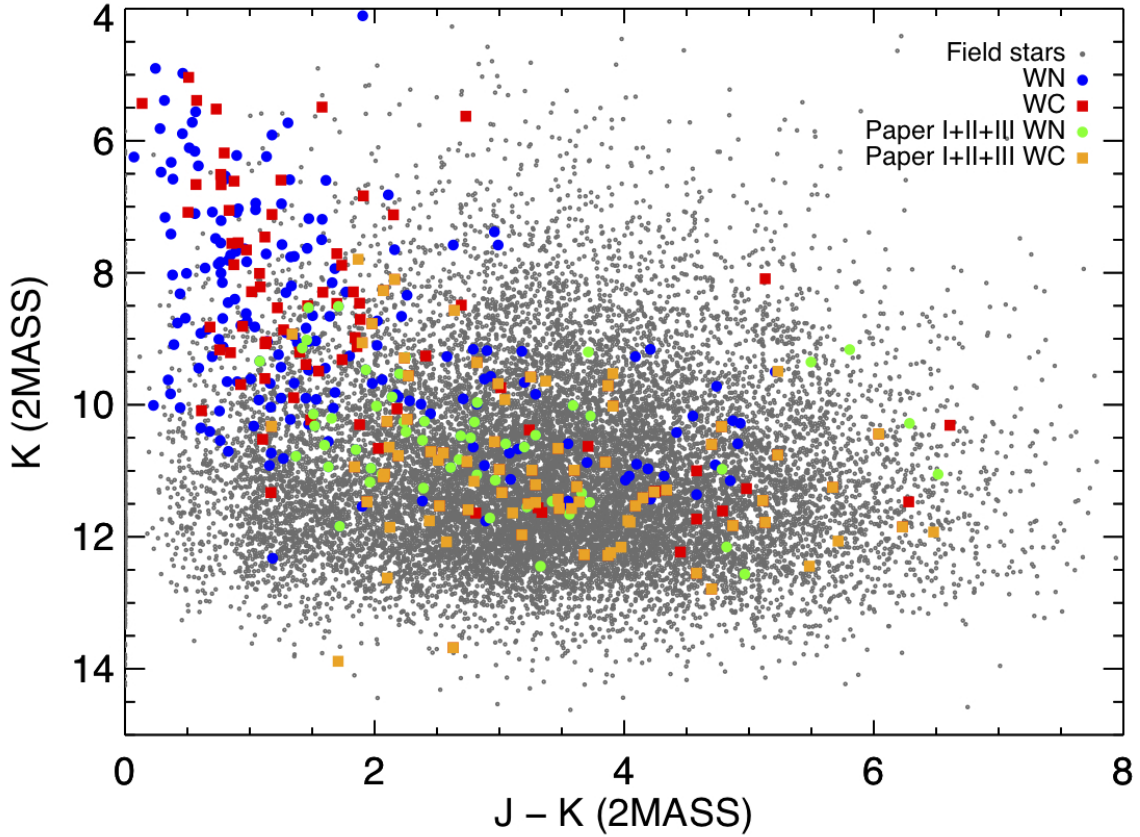


Fig. 27.— NIR color-magnitude diagram, using 2MASS magnitudes of field and WR stars. This diagram demonstrates that the Shara et al survey is probing a more distant population of WRs than previous methods. The WRs we have identified are significantly fainter and redder than those in the literature, and would have been lost among the field stars by other selection methods.